

1
2
3
4
5
6
7
8
9
10
11
12
13
14
15
16
17
18
19
20
21
22
23

Size-Resolved Dust Direct Radiative Effect Efficiency

Derived from Satellite Observations

Qianqian Song^{1,2,*}, Zhibo Zhang^{1,2}, Hongbin Yu³, Jasper F. Kok⁴, Claudia Di Biagio⁵,
Samuel Albani⁶, Jianyu Zheng^{1,2}, Jiachen Ding⁷

1. Physics Department, UMBC, Baltimore, Maryland, USA
2. Goddard Earth Sciences Technology and Research II, UMBC, Baltimore, Maryland, USA
3. Climate and Radiation Laboratory, NASA Goddard Space Flight Center, Greenbelt, Maryland, USA
4. Department of Atmospheric and Oceanic Sciences, University of California, Los Angeles, CA 90095, USA
5. Université Paris Cité and Univ Paris Est Creteil, CNRS, LISA, F-75013 Paris, France
6. Department of Environmental and Earth Sciences, University of Milano-Bicocca, Milan, Italy
7. Department of Atmospheric Sciences, Texas A&M University, College Station, Texas, USA

*Correspondence to: Qianqian Song

Email: cd11735@umbc.edu

24 **Abstract**

25 The role of mineral dust aerosol in global radiative energy budget is often quantified by
26 the dust direct radiative effect (DRE). The dust DRE strongly depends on dust aerosol optical
27 depth (DAOD), therefore, DRE efficiency ($DREE=DRE/DAOD$) is widely compared across
28 different studies to eliminate difference due to the various dust load. Nevertheless, DREE is still
29 influenced by the uncertainties associated with dust particle size distribution (PSD) and optical
30 properties. In this study, we derive a global clear-sky *size-resolved* DREE dataset in both
31 shortwave (SW) and longwave (LW) at top of the atmosphere (TOA) and surface based on satellite
32 observations (i.e., satellite-retrieved dust extinction spatial and vertical distributions). In the DREE
33 dataset, dust geometric diameter from $0.1\mu\text{m}$ to $100\mu\text{m}$ is divided into 10 bins and the
34 corresponding monthly mean DREE (with respect to DAOD at 532nm) for each size bin is derived
35 by using the Rapid Radiative Transfer Model (RRTM). Three sets of state-of-the-art dust refractive
36 indices (RI) and two sets of dust shape models (sphere vs. spheroid) are adopted to investigate the
37 sensitivity of dust DREE to dust absorption and shape. As a result, the size-resolved dust DREE
38 dataset contains globally distributed monthly mean dust DREE at TOA and surface for each of 10
39 size bins with 5° (longitude) \times 2° (latitude) resolution as well as for each dust RI and shape
40 combination. The size-resolved dust DREE dataset can be used to readily calculate global dust
41 DRE for any DAOD and dust PSD, including the uncertainty in the DRE induced by dust
42 microphysical properties (e.g., dust PSD, RI and shape). By calculating dust DRE based on DAOD
43 climatology retrieved from different satellite sensors and based on different dust PSD, we find that
44 uncertainty in the spatial pattern of DAOD induces more than 10% of the uncertainty in SW dust
45 DRE at TOA. The observation-based dust PSD induces around 15%~20% uncertainty in dust DRE
46 at TOA and in the atmosphere. The sensitivity assessments of dust DRE to dust RI and shape

47 further suggest that dust non-sphericity induces a negligible effect on dust DRE estimations, while
48 dust RI turns out to be the most important factor in determining dust DRE, particularly in SW.
49

50

51 **1 Introduction**

52 Mineral dust is an important component of the atmospheric aerosol (Textor et al., 2006;
53 Choobari et al., 2014). They can influence the radiative energy budget of the Earth-Atmosphere
54 system directly through their interaction with both solar and thermal infrared radiation, which is
55 known as the direct radiative effect (DRE) of dust. The DRE of dust consists of two components.
56 In the solar shortwave (SW) spectral region, dust aerosols reflect a fraction of solar radiation back
57 to the space which generally leads to a negative cooling effect at both top of the atmosphere (TOA)
58 and surface (Tegen et al., 1996; Myhre et al., 2003). In the longwave (LW) thermal infrared region,
59 dust aerosols trap the thermal radiation emitted from Earth's surface by absorption, which
60 generally leads to a positive warming radiative effect at TOA and surface (Sokolik et al., 1998).
61 In addition to DRE, dust can also influence the radiation and the hydrological cycles indirectly
62 through serving as cloud condensation nuclei and ice nuclei and affecting cloud microphysical
63 properties and cloud lifetime, known as indirect effects of dust (Twomey, 1977; Albrecht, 1989).

64 The dust DRE depends on many factors including primarily the atmospheric dust content,
65 represented by its optical depth (DAOD), vertical distribution (especially important for LW DRE),
66 and particles' physico-chemical properties that are the particle size distribution (PSD), complex
67 refractive index (RI), and shape. Besides dust PSD, RI and shape, the dust DRE also depends on
68 the atmospheric composition and structure, notably the atmospheric vertical profile of clouds,
69 water vapor, and temperature, as well as surface properties (Yu et al., 2006). All of these properties
70 vary in space and time and need to be characterized at the best possible spatio-temporal resolution
71 in order to get realistic dust DRE estimates.

72 Among all these factors, DAOD is of first order importance in determining dust DRE since
73 dust DRE is approximately linear with DAOD (Satheesh and Ramanathan, 2000). Many previous
74 studies related to dust DRE are based on DAOD distributions from model simulations. For
75 example, Kok et al. (2017) used four global model simulations to estimate global mean dust DRE
76 efficiency (DREE is defined as $DRE/DAOD$) and further derive global mean dust DRE. Di Biagio
77 et al. (2020) derived dust DRE based on model-simulated DAOD distributions with global annual
78 mean DAOD constrained by observations. The main advantage of these studies is the availability
79 of continuous and detailed DAOD spatial and temporal variation from model simulations. On the
80 other hand, model-simulated DAOD could be subject to large uncertainties and biases in
81 reproducing DAOD due to parameterizations of various physical processes, therefore need
82 observational constraints for evaluation and improvement.

83 Satellite observations are important sources of data for evaluating model simulations,
84 because of their routine sampling on a global scale and over decadal time periods. Previous studies
85 have developed sensor-specific methods to distinguish dust aerosol from total aerosol based on the
86 size and shape characteristics of dust particles. Some are based on passive satellite observations
87 such as Moderate Resolution Imaging Spectroradiometer (MODIS, Remer et al. (2005)) and others
88 are based on active observations such as Cloud-Aerosol Lidar with Orthogonal Polarization
89 (CALIOP, Winker et al. (2009)). The wide spectral coverage of MODIS measurements allows the
90 retrieval of aerosol particle size information, such as effective radius, fine-mode fraction, aerosol
91 Angstrom exponent, as well as spectral gradient of absorption (Remer et al., 2005; Hsu et al., 2013).
92 Based on the fact that dust aerosols are generally larger in size than other aerosols and have a
93 decreasing absorption from ultraviolet (UV) to the near infrared, the combinations of these
94 retrievals provide the basis for dust separation and dust aerosol optical depth (DAOD) retrievals

95 from MODIS (Kaufman et al., 2005; Ginoux et al., 2012; Voss and Evan, 2020; Yu et al., 2009,
96 2019). In addition, some recent studies have also characterized dust distribution through
97 integrating MODIS measurements with other data sources and model simulations, for example,
98 using the DAOD-to-AOD ratio from MERRA-2 (Modern-Era Retrospective analysis for Research
99 and Applications, version 2), Gkikas et al. (2021) converted the MODIS AOD retrievals to DAOD.
100 However, passive sensors do not provide the vertical structure of aerosol that is critical for studying
101 aerosol–cloud interactions, LW radiative effects and aerosol influences on the thermal structure of
102 the atmosphere (e.g., Meloni et al., 2005, 2015). By contrast, the active sensor CALIOP can
103 provide the vertical profiles of aerosol extinction and particle properties such as depolarization
104 ratio and color ratio, which have been used for improving DAOD retrievals in thermal infrared
105 (TIR) (Zheng et al., 2022) and evaluating global dust simulations (Yu et al., 2010; Wu et al., 2020).
106 The CALIOP dust identification is mainly based on dust aerosols being non-spherical in shape and
107 their linear depolarization ratio being much larger than spherical aerosols (Sakai et al., 2010).

108 Using CALIOP retrievals, Song et al. (2021) derived a three-dimensional (3D) decadal
109 (2007-2019) global scale dust extinction profile climatology, which provides an observational
110 constraint on both the spatial DAOD pattern and the vertical dust distribution for studying dust
111 DRE and evaluating models. In their study, Song et al. (2021) also compared dust retrievals, in
112 particular DAOD, based on different methods (i.e., CALIOP-based and MODIS-based DAOD
113 retrievals), showed that DAOD often differ significantly between the different products and further
114 discussed the potential reasons of causing the differences (e.g., instrument calibration errors and
115 errors in discriminating cloud from aerosol, globally uniform dust Lidar Ratio assumption in
116 CALIOP DAOD retrieval and so on). They showed that DAOD derived from CALIOP
117 observations is generally smaller and more concentrated over ‘dust belt’ regions - extending from

118 the west coast of north Africa to the Middle East, central Asia, and China - than that derived from
119 MODIS observations. These differences in DAOD in turn lead to different dust DRE estimations,
120 making it difficult to compare different studies to reach meaningful conclusions. Even an
121 agreement of DRE could be a result of the compensation between differences in DAOD and other
122 aforementioned factors, such as dust microphysical properties. Therefore, DRE provides only a
123 weak constraint on model. Instead, a normalized quantity, DRE efficiency (DREE) as the ratio of
124 DRE to DAOD, has been widely used in inter-comparison studies and model evaluations (Di
125 Biagio et al. 2020). Because of the elimination of DAOD, the DREE provides a stronger constraint
126 on dust microphysical properties and their impacts on the dust DRE from different dust source
127 regions (García et al., 2008).

128 In addition to DAOD, dust size is also an important factor in determining dust DRE
129 (Mahowald et al., 2014). Smaller particles are more effective at scattering SW radiation and super-
130 micron particles are more effective at absorbing both SW and LW radiation (Tegen and Lacis,
131 1996). Therefore, when other parameters are equal, fine dust would generally have a more negative
132 SW DRE and a less positive LW DRE than coarse dust. Unfortunately, despite its importance, the
133 simulation of dust PSD in the models and satellite retrievals of dust size remain challenging tasks
134 (Ryder et al., 2019). As a result, there is a large uncertainty in our understanding of dust PSD. For
135 example, several recent studies suggested that model simulations tend to underestimate dust size,
136 especially the very coarse dust with diameter in excess of 5 μm (Adebisi and Kok, 2020).
137 Moreover, dust RI and shape can be important for DRE estimation as well because besides dust
138 PSD they are the other two factors that determine dust spectral optical properties. As such, it is
139 important to investigate the sensitivity of dust DRE to dust PSD, RI and shape. Previous studies
140 suggest that large dust PSD and RI uncertainty leads to a large uncertainty in dust DRE and thereby

141 DREE estimations. For example, Song et al., (2018) shows that the SW DREE of a dust model
142 with a large size and less absorptive RI is very similar to that of a dust model with a smaller size
143 and more absorptive RI, both in the range of satellite derived values in the NE Atlantic region. Not
144 surprisingly, even DREE cannot provide sufficient constraints due to this possible compensation
145 of effects in the dust PSD and RI.

146 The main objective of this study is to derive a global clear-sky size-resolved dust DREE
147 dataset based on satellite observations and demonstrate its usefulness in constraining, comparing,
148 and understanding the dust DRE estimations. As explained below, the size-resolved DREE
149 decomposes the DREE of dust into several size bins and therefore provide a way to take into
150 account the effects of dust PSD explicitly. The sensitivity of dust DRE to dust RI and shape are
151 also assessed in this study. Due to the inhomogeneous spatio-temporal distribution of those
152 aforementioned factors, it is thus important to consider the spatio-temporal variation of dust DREE.
153 Therefore, we organize the DREE dataset at 5° (longitude) \times 2° (latitude) horizontal resolution
154 and at monthly temporal resolution. To the best of our knowledge, this work presents the first such
155 dataset based on retrieved dust properties (i.e., DAOD vertical and horizontal distributions) from
156 satellite observations, although size-resolved DREE from model simulations have been used in
157 previous studies. We will show that our size-resolved DREE can allow users to readily compute
158 the DREE and DRE of dust based on any dust PSD (e.g., from model simulations, satellite
159 retrievals or in-situ measurements). We will also carry out an inter-comparison of the global dust
160 DRE estimations based on different dust PSD and compare the results with previous studies. With
161 these functions, we expect that the size-resolved DREE will be a useful tool for both observational
162 and modeling studies of dust DRE.

163 The rest of the paper is organized as follows. Section 2 provides a description of the data
164 and models used in this study. Section 3 describes the methodology of deriving the size-resolved
165 DREE dataset. In section 4, we describe a methodology of calculating the dust DRE with the size-
166 resolved DREE dataset and its validation. In section 5, we compare the regional and global dust
167 DRE estimations based on different DAOD, dust PSD and compare the results with previous
168 studies. Section 6 provides a summary of the study along with the main conclusions.

169 **2 Data and Models**

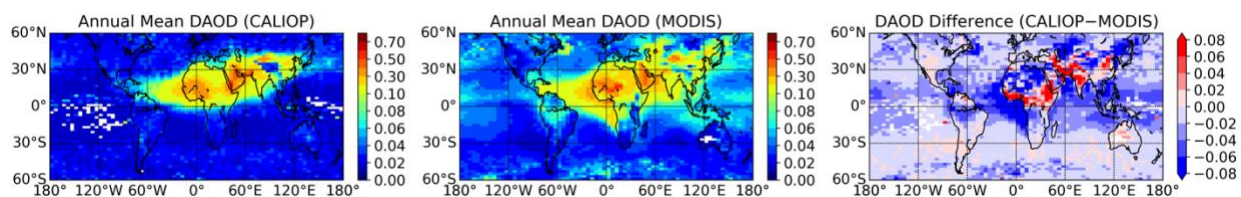
170 **2.1 Satellite-based DAOD climatology**

171 We use CALIOP-based DAOD climatology and dust vertical distribution derived in Song
172 et al. (2021) to derive a size-resolved dust DREE. The reason for choosing CALIOP-based DAOD
173 climatology is discussed in detail in section 3.2. The CALIOP-based dust climatology dataset
174 contains monthly mean DAOD and dust vertical extinction profile on a 5° (longitude) \times 2°
175 (latitude) spatial resolution grid for the period 2007-2019. The CALIOP-based DAOD and dust
176 vertical distribution climatology from 2007 to 2010 are used to derive monthly mean size-resolved
177 dust DREE dataset in this study. The selection of 4 years (2007-2010) for DREE calculations is
178 based on several considerations. Firstly, the multi-year DREE calculations allow us to investigate
179 the effect of interannual variations of atmospheric and surface properties to dust DRE. Secondly,
180 this selection is consistent with Song et al. (2018), making it easier to compare our results with
181 previous work. Thirdly, considering the computational efficiency, we do not extend the calculation
182 to more years.

183 In addition to CALIOP-based DAOD climatology, we will use the MODIS-based DAOD
184 climatology to investigate the sensitivity of dust DRE to DAOD spatial pattern in section 5.2. The
185 MODIS-based DAOD climatology achieves global coverage on a 5° (longitude) \times 2° (latitude)

186 spatial resolution for the period 2003-2019 by combining the monthly mean Aqua MODIS over-
 187 ocean (Yu et al., 2020) and over-land (Pu and Ginoux, 2018) DAOD. In contrast to CALIOP-based
 188 DAOD climatology which is based on dust non-sphericity to separate dust aerosol from CALIOP
 189 total aerosol observations, MODIS-based DAOD retrieval is mainly based on dust large size to
 190 partition DAOD from MODIS total aerosol observations. The two sensor-specific dust partition
 191 methods result in different DAOD magnitude and spatial pattern retrievals.

192 Figure 1 shows annual mean DAOD from 2007 to 2010 based on CALIOP and MODIS
 193 observations. CALIOP-based and MODIS-based DAOD climatology differ in terms of both
 194 magnitude and spatial pattern. MODIS-based DAOD is generally larger than CALIOP-based
 195 DAOD. For example, the global ($60^{\circ}S - 60^{\circ}N$) 4-year mean MODIS-based DAOD is 0.047, while
 196 CALIOP-based DAOD is 0.032. High DAOD are seen from both CALIOP-based and MODIS-
 197 based DAOD over the ‘dust belt’ regions, where large-scale dust activities occur persistently
 198 throughout the year. However, the CALIOP-based DAOD is rather low in some other regions that
 199 are known to be dusty in certain seasons, such as South America, Australia, and South Africa. In
 200 other words, the two satellite-based DAOD spatial pattern differs significantly with CALIOP-
 201 based DAOD more concentrated over ‘dust belt’ regions.



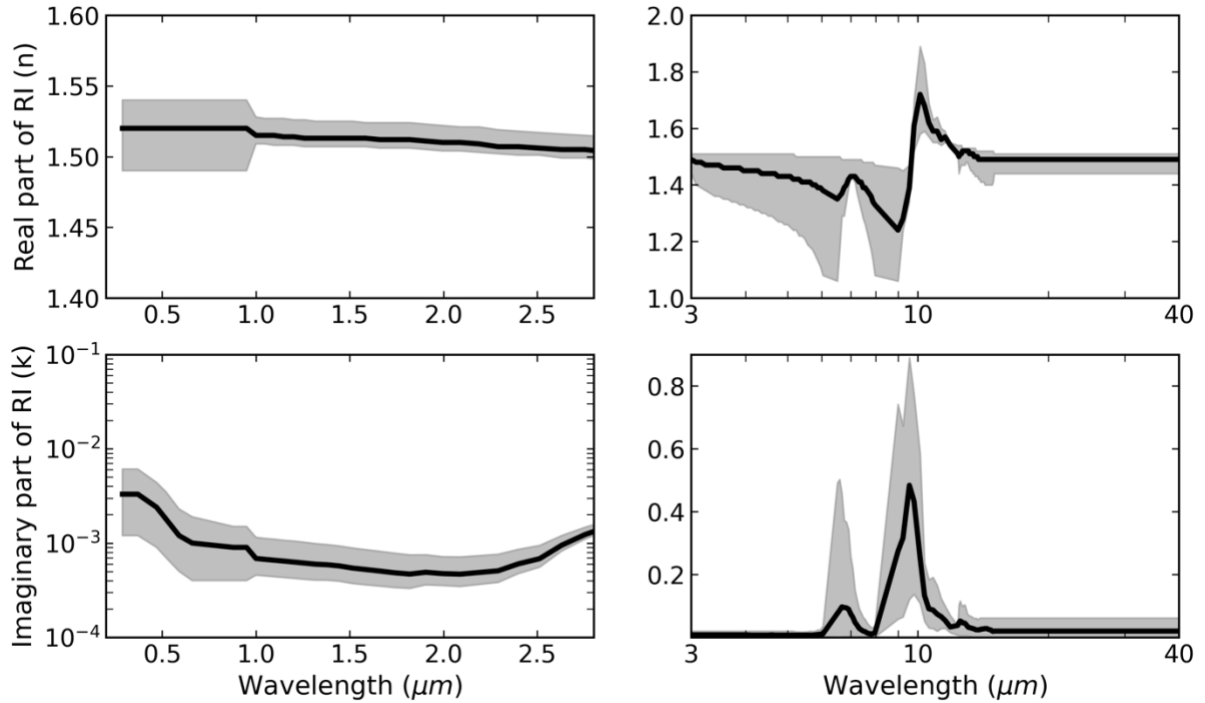
202
 203 Figure 1. Global ($60^{\circ}S - 60^{\circ}N$) spatial pattern of CALIOP-based and MODIS-based 4-year (2007-2010) mean
 204 DAOD (Song et al., 2021) and their difference.

205 2.2 Dust physical and optical models

206 To study the sensitivity of dust DREE to dust RI and dust shape, we adopt three sets of
 207 dust RI (Figure 2) and two dust shapes and compute a total of 6 sets of DREE based on their

208 combinations. The three dust RI sets represent less absorptive, mean absorptive and more
209 absorptive dust aerosols and the two dust shapes include spherical and spheroidal dust shapes (dust
210 shape distribution is shown in Figure 4 (a) in Song et al. 2018). The mean, 10th and 90th percentile
211 of calculated RI for 19 dust samples over 8 regions in Di Biagio et al. (2019) are used to represent
212 mean, less and more absorptive dust in SW. We combine RI of wavelengths from 0.37 μ m to
213 0.95 μ m measured in Di Biagio et al. (2019) and RI of other wavelengths up to 3 μ m reported in
214 Balkanski et al. (2007) to get full spectral coverage in SW. The mean, minimum and maximum RI
215 of wavelengths beyond 3 μ m measured in Di Biagio et al. (2017) are used to represent mean, less
216 and more absorptive dust in LW. Two dust shapes are used to investigate the effect of dust
217 nonsphericity on dust DRE. One is spherical dust shape, the other one is spheroidal dust shape
218 with dust aspect ratio distribution described by Figure 4 (a) in Song et al. (2018) which is originally
219 from Dubovik et al. (2006). Each combination of dust RI and dust shape is considered as a dust
220 model. As a result, the three dust RI and two dust shapes constitute six dust models in SW and
221 LW, respectively, as shown in Table 1.

222



223

224 Figure 2. The SW and LW spectral refractive indices (RI) used in this study obtained from Di Biagio et al. (2017,2019)
 225 and Balkanski et al. (2007). The black curves represent the mean RI which indicates the mean absorptive dust. The
 226 grey shading represents the upper and lower limits indicating more absorptive and less absorptive dust, respectively.

227 Table 1. Dust models used in this study. Three dust RI are used in shortwave (SW) and longwave (LW) to represent
 228 less, mean, and more absorptive dust, respectively. Two dust shape models are used to represent spherical and
 229 spheroidal dust shape. The three dust RI sets and two dust shapes constitute 6 dust models in SW and LW respectively.

	SW RI (Balkanski et al. 2007; Di Biagio et al. 2019)			LW RI (Di Biagio et al. 2017)		
	10%	Mean	90%	Minimum	Mean	Maximum
Sphere	MinSWRI-Sphere	MeanSWRI-Sphere	MaxSWRI-Sphere	MinLWRI-Sphere	MeanLWRI-Sphere	MaxLWRI-Sphere
Spheroid	MinSWRI-Spheroid	MeanSWRI-Spheroid	MaxSWRI-Spheroid	MinLWRI-Spheroid	MeanLWRI-Spheroid	MaxLWRI-Spheroid

230

231 3 Methodology

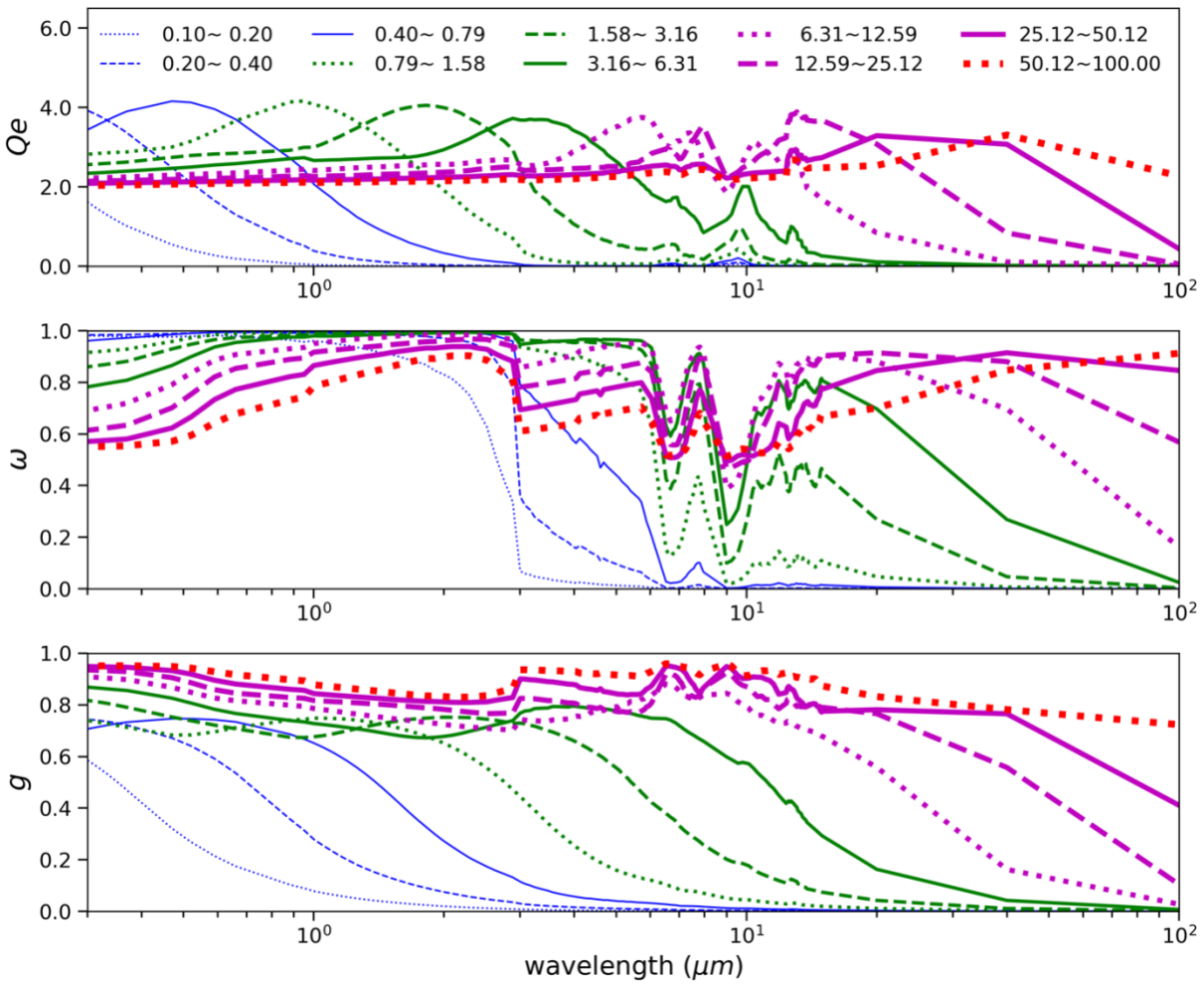
232 3.1 Size-resolved dust scattering properties

233 Rapid Radiative Transfer Model (RRTM) (Mlawer et al., 1997) is used to compute both
 234 SW and LW radiative fluxes for both clean (i.e., cloud-free and aerosol-free) and dusty
 235 atmospheres (i.e., free of clouds and non-dust aerosols). RRTM retains reasonable accuracy in

236 comparison with line-by-line results for single column calculations (Mlawer and Clough, 1998;
237 Mlawer et al., 1997). It divides the solar spectrum into 14 continuous bands ranging from 0.2 to
238 12.2 μm and the thermal infrared (3.08–1000 μm) into 16 bands. We explicitly specify the spectral
239 DAOD, single scattering albedo (ω), and asymmetry parameter (g) of dust aerosols for every band
240 in the RRTM radiative transfer simulations. In contrast to radiative transfer scheme in most global
241 models, which do not account for LW scattering, scattering capability is available through the
242 discrete-ordinate-method radiative transfer (DISORT) in RRTM_LW (Stamnes et al., 1988). Four
243 streams are used in DISORT. The Henyey-Greenstein phase function is used and only the first
244 moment of the phase function (i.e., asymmetry parameter) needs to be specified in the RRTM.

245 Dust scattering properties (extinction efficiency Q_e , ω and g) depend on several factors
246 including dust PSD, RI, and dust shape. To account for the impact of dust PSD, we divide dust
247 diameters into 10 logarithmically spaced size bins. The 10 size bins represent a wide range of dust
248 geometric diameters (i.e., diameter of a sphere with the same volume) ranging from 0.1 μm to
249 100 μm . The geometric diameter (hereafter diameter or D) range of each size bin is listed in Figure
250 3. For each size bin k , the spectral scattering properties (Qe_k^λ , ω_k^λ and g_k^λ) are calculated for each
251 dust model shown in Table 1 and each spectral band. In the calculations of scattering properties
252 (Qe_k^λ , ω_k^λ and g_k^λ), dust particle number (dN/dD) is assumed to be uniformly distributed within
253 each size bin. We use the Lorenz–Mie theory code of Wiscombe (1980) to compute the spectral
254 optical properties of dust particles in the assumption of sphericity. The spectral optical properties
255 of spheroidal dust particles are derived from the database of Meng et al. (2010). Figure 3 shows
256 Qe_k^λ , ω_k^λ and g_k^λ for MeanSWRI-MeanLWRI-Spheroid dust model. In SW, finer dust has a larger
257 ω and smaller g , implying a more effective SW backscattering of finer dust. As a result, finer dust
258 is expected to have stronger cooling effect (more negative DREE values) at TOA generally. In

259 LW, $\frac{Qe_k^{10\mu m}}{Qe_k^{532nm}}$ is generally enhanced as dust size increases, which implies that coarser dust has larger
 260 extinction in LW (optically represented by $DAOD^{10\mu m}$) than finer dust when $DAOD^{532nm}$ is
 261 constrained by CALIOP retrieval. As a result, larger $DAOD^{10\mu m}$ will enhance the LW warming
 262 (more positive LW DREE) at TOA of coarser size bins. On the other hand, the increased ω and g
 263 of the coarser size bins indicates stronger forward scattering, which reduces the enhancement in
 264 LW warming induced by larger $DAOD^{10\mu m}$.



265
 266 Figure 3. Spectral scattering properties (i.e., Q_e : extinction efficiency, ω : single scattering property, g : asymmetry
 267 parameter) of each size bin for the MeanSWRI-MeanLWRI-Spheroid dust model. The scattering properties of each
 268 size bin are represented by the corresponding curve indicated in the legend. Each size bin is defined with respect to
 269 dust diameter with unit of micrometers (μm).

270 3.2 DREE dataset

271 Based on the dust scattering properties shown in Figure 3 and the procedures summarized
272 in Figure 4, we compute the size-resolved dust DREE for the MeanSWRI-MeanLWRI-Spheroid
273 dust model in SW and LW. In this section, we focus on demonstrating the method of deriving size-
274 resolved dust DREE for one dust model, but this method is applicable to all six dust models listed
275 in Table 1.

276 First, we use RRTM to simulate monthly mean dust DRE from 2007 to 2010 for each 5°
277 (longitude) \times 2° (latitude) grid with CALIOP-based $DAOD^{532nm}$ exceeding 0.01. The
278 $DAOD^{532nm} \geq 0.01$ threshold ensures most dusty regions over the globe are covered (see Figure
279 S1 and Figure S2 in the Supplement) and in the meanwhile balances the computational cost. Dust
280 DRE are calculated for each size bin using the extinction properties of the corresponding size bin
281 shown in Figure 3 (denoted as $DRE_{k,i,j}$, hereafter k indicates size bin index and (i,j) indicates
282 longitude-latitude grid index, unless specified otherwise). Note that we do not consider dust RI
283 spatial variation and dust size vertical variation due to the lack of observation-based dust
284 minerology and size estimation on global scale. In $DRE_{k,i,j}$ calculations, we constrain the monthly
285 mean dust extinction vertical distributions using the CALIOP-based climatological dataset of Song
286 et al. (2021). Worth to mention, our target in this section is $DREE_{k,i,j}$ calculations. Considering
287 dust DRE is approximately linear to DAOD (Satheesh and Ramanathan, 2000), the DAOD used
288 in dust DRE calculations will not affect dust DREE results significantly, we simply calculate dust
289 $DRE_{k,i,j}$ with respect to $DAOD_{i,j}^{532nm}$ from CALIOP-based DAOD climatology. As a result,
290 $DRE_{k,i,j}$ calculated in this section are only intermediate variables used to calculate dust DREE,
291 they do not represent actual DRE contributed by k^{th} size bin. The atmospheric profiles such as
292 water vapor (H_2O), ozone (O_3) and temperature (T_{atm}) vertical profiles of 72 levels are from 3-

293 hourly MERRA2 assimilated meteorological fields data (Gelaro et al., 2017). We combine the 1-
 294 hourly surface albedo for visible beam from MERRA2 radiation diagnostics with the instantaneous
 295 spectral surface albedo from the integrated CALIPSO, Cloud-Sat, CERES, and MODIS merged
 296 product (CCCM) (Kato et al., 2011) to get time-dependent spectral surface albedo. Surface
 297 temperature is obtained from 1-hourly MERRA2 radiation diagnostics data. The atmospheric and
 298 surface properties are all aggregated to monthly mean values at eight UTC times: 0:30, 3:30, 6:30,
 299 9:30, 12:30, 15:30, 18:30, 21:30 to obtain monthly-mean diurnal cycle for radiative transfer
 300 simulations. Considering DRE^{SW} strongly depends on solar zenith angle (SZA), we calculate
 301 DRE^{SW} for every 1 hour using the corresponding hourly SZA in midmonth day. As a result, every
 302 three SZA share the same atmospheric and surface properties in DRE^{SW} calculations due to their
 303 different temporal resolution.

304 Table 2 List of definitions of variables and their indices.

Variable	Definition
k	size bin index
i, j	longitude-latitude grid index
t	8 UTC times with 3-hour interval (i.e., 0:30, 3:30, 6:30, 9:30, 12:30, 15:30, 18:30, 21:30)
tt	24 UTC times with 1-hour interval
day ^{mm}	The midmonth day of the month
$\overline{R(t), H_2O(t), O_3(t), CO_2(t), T_{atm}(t)}$	3-hourly monthly mean surface albedo and vertical profile of water vapor, ozone, carbon dioxide and atmospheric temperature
ζ_d	dust properties such as DAOD, dust extinction vertical profile and scattering properties
$\overline{{}_{1h}DRE_{k,i,j}^{SW}(tt)}$	1-hourly monthly mean DRE^{SW} (i.e., monthly mean DRE^{SW} at each of 24 UTC times) of k^{th} size bin and (i^{th} , j^{th}) grid
$\overline{{}_{3h}DRE_{k,i,j}^{LW}(t)}$	3-hourly monthly mean DRE^{LW} (i.e., monthly mean DRE^{LW} at each of 8 UTC times) of k^{th} size bin and (i^{th} , j^{th}) grid
$\overline{DRE_{k,i,j}^{SW}, DRE_{k,i,j}^{LW}}$	The monthly and diurnally mean dust DRE^{SW} and DRE^{LW} of k^{th} size bin and in (i^{th} , j^{th}) grid
$\overline{DREE_{k,i,j}}$	The monthly and diurnally mean dust $DREE^{SW}$ and $DREE^{LW}$ of k^{th} size bin and (i^{th} , j^{th}) grid
$\overline{DAOD_{i,j}^{532nm}}$	The monthly mean dust optical depth at 532nm of (i^{th} , j^{th}) grid

305
 306 The definitions of variables and indices used to derive size-resolved dust DREE dataset are
 307 summarized in Table 2. Eq. (1) shows the way of deriving 1-hourly monthly mean DRE^{SW} .

$$\overline{{}_1hDRE_{k,i,j}^{SW}(tt)} = DRE_{k,i,j}^{SW}(\overline{R(t)}, \overline{H_2O(t)}, \overline{O_3(t)}, \overline{CO_2(t)}, \zeta_d, \overline{SZA(day^{mm}, tt)}), \quad (1)$$

308 where ‘ t ’ indicates 8 UTC times with 3-hour interval. ‘ tt ’ indicates 24 UTC times with 1-hour
 309 interval. ‘ day^{mm} ’ indicates the midmonth day of the month, and ‘ $\overline{R(t)}$ ’ represents 3-hourly
 310 monthly mean surface albedo. We include 3-hourly monthly mean vertical profile of water vapor,
 311 ozone, carbon dioxide ($\overline{H_2O(t)}$, $\overline{O_3(t)}$, $\overline{CO_2(t)}$) to account for gaseous absorption. The temporal
 312 resolution inconsistency of SZA as well as atmospheric and surface properties requires every three
 313 SZA share the same atmospheric and surface properties in the calculations. ‘ ζ_d ’ represents dust
 314 properties such as DAOD, dust extinction vertical profile and scattering properties which are
 315 independent of UTC time in our calculations. Dust extinction vertical profile is interpolated to the
 316 72 levels in consistency with vertical profiles of water vapor, ozone and temperature from
 317 MERRA2.

318 Eq. (2) shows the way of deriving 3-hourly monthly mean DRE^{LW} .

$$\overline{{}_3hDRE_{k,i,j}^{LW}(t)} = DRE_{k,i,j}^{LW}(\overline{E}, \overline{H_2O(t)}, \overline{O_3(t)}, \overline{CO_2(t)}, \overline{T_{atm}(t)}, \zeta_d) \quad (2)$$

319 Surface spectral emissivity (‘ E ’) is obtained from Huang et al. (2016), which contains
 320 monthly mean spectral surface emissivity with 0.5-degree spatial resolution based on MODIS-
 321 retrieved mid-IR surface emissivity and modeled different types of surface spectral emissivity.
 322 $\overline{T_{atm}(t)}$ represents 3-hourly monthly mean vertical profile of atmospheric temperature. With the
 323 aid of the 3-hourly monthly mean atmospheric properties, monthly mean DRE^{LW} is calculated for
 324 every 3 hours.

325 Then the 1-hourly monthly mean dust DRE^{SW} ($\overline{{}_1hDRE_{k,i,j}^{SW}(tt)}$) derived from Eq. (1) is
 326 averaged diurnally (over 24 points) to get the monthly and diurnally mean dust DRE^{SW} ($\overline{DRE_{k,i,j}^{SW}}$)
 327 as indicated by Eq. (3).

$$\overline{DRE_{k,i,j}^{SW}} = \frac{\overline{\sum_{tt} 1h DRE_{k,i,j}^{SW}(tt)}}{\sum tt} \quad (3)$$

328

329 Similarly, the 3-hourly monthly mean DRE^{LW} ($\overline{3h DRE_{k,i,j}^{LW}(t)}$) derived from Eq. (2) is
 330 averaged diurnally (over 8 points) to get the monthly and diurnally mean dust DRE^{LW} ($\overline{DRE_{k,i,j}^{LW}}$) as
 331 indicated by Eq. (4).

$$\overline{DRE_{k,i,j}^{LW}} = \frac{\overline{\sum_t 3h DRE_{k,i,j}^{LW}(t)}}{\sum t} \quad (4)$$

332 The method described by Eq. (1) - Eq. (4) will be referred to as the ‘*conventional*’ method
 333 of calculating monthly mean dust DRE in Section 4.

334 Based on the monthly mean size-resolved dust DRE^{SW} ($\overline{DRE_{k,i,j}^{SW}}$) and DRE^{LW} ($\overline{DRE_{k,i,j}^{LW}}$), we
 335 derive the monthly mean size-resolved dust DREE ($\overline{DREE_{k,i,j}}$) using Eq. (5) for SW and LW
 336 respectively. Note that the monthly mean size-resolved dust DREE ($\overline{DREE_{k,i,j}}$) is calculated by
 337 dividing by monthly mean $DAOD^{532nm}$ since the size-resolved $\overline{DRE_{k,i,j}}$ was initially derived with
 338 respect to monthly mean $DAOD^{532nm}$.

$$\overline{DRE_{k,i,j}^{SW \text{ or } LW}} = \frac{\overline{DRE_{k,i,j}^{SW \text{ or } LW}}}{\overline{DAOD_{i,j}^{532nm}}} \quad (5)$$

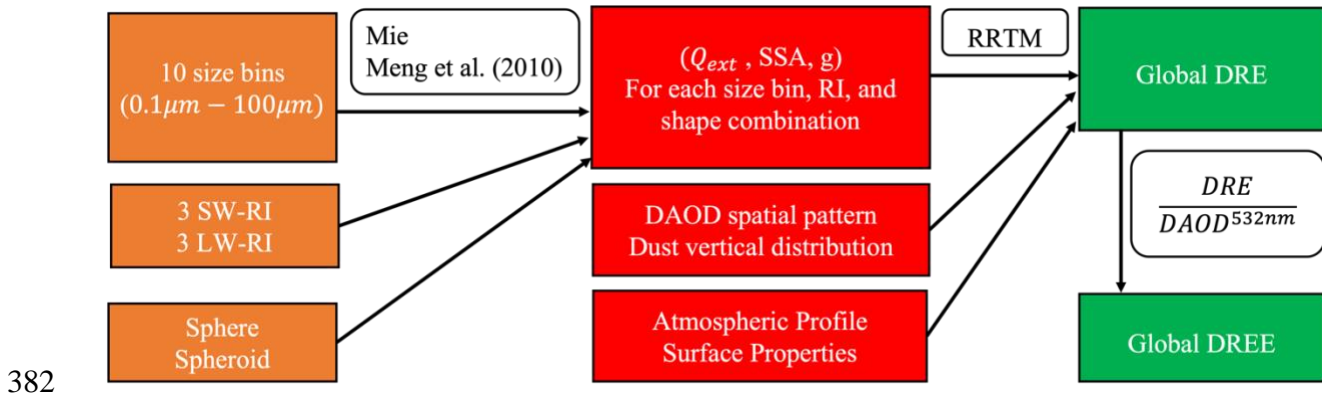
339 Finally, we average the monthly mean size-resolved dust DREE ($\overline{DREE_{k,i,j}}$) over 4 years
 340 to get monthly mean size-resolved dust DREE datasets in addition to the associated interannual
 341 standard deviation (std). The std indicates the DREE uncertainty caused by interannual variation
 342 of monthly mean atmospheric and surface properties as well as dust vertical distribution. Finally,
 343 the dataset developed in this study contains monthly mean size-resolved dust DREE and its
 344 associated interannual std at TOA and surface with dimension of 10 bins, 12 months, 90 latitudes,

345 72 longitudes for each of six dust models in SW and LW respectively. Figure S1 and Figure S2 in
346 the Supplement demonstrate the global distribution of the monthly mean size-resolved DREE^{SW}
347 and DREE^{LW} at TOA for June.

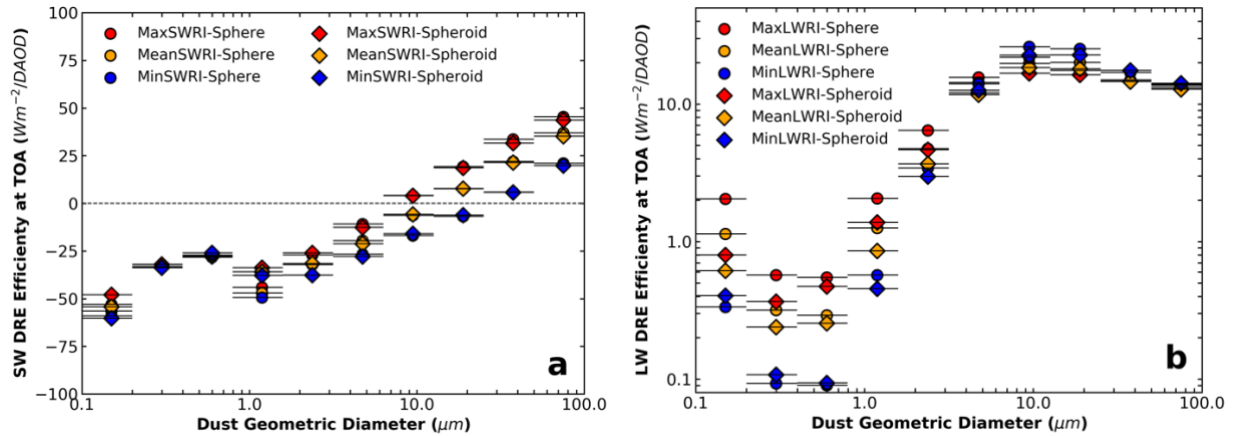
348 It is important to note that dust DREE of each grid cell rarely depends on the DAOD
349 because dust DRE is approximately linear with DAOD (Satheesh and Ramanathan, 2000).
350 Therefore, the choice of CALIOP- or MODIS-based DAOD climatology to derive the global
351 ($5^\circ \times 2^\circ$) size-resolved DREE dataset will not lead to large difference. In other words, the size-
352 resolved DREE dataset is rarely related to the robustness of the DAOD used in the derivation
353 process. We select CALIOP-based DAOD to derive the size-resolved dust DREE dataset because
354 that the CALIOP-based dust climatology contains dust vertical distribution, which is especially
355 important for obtaining LW DREE. Nevertheless, using CALIOP-based dust retrieval to derive
356 size-resolved dust DREE dataset has several limitations: (1) The size-resolved dust DREE dataset
357 may miss some regions with tenuous dust layers that below the CALIOP sensitivity. (2) The LW
358 DREE is related to the quality of dust vertical distribution retrieval. By contrast, dust DRE highly
359 depends on DAOD, therefore we will use different DAOD climatological datasets retrieved from
360 different sensors (i.e., CALIOP and MODIS) to investigate global dust DRE in section 5.2.
361 Furthermore, even though dust DREE of each grid cell is rarely related to DAOD, regional or
362 global mean dust DREE will depend on the DAOD spatial distribution (i.e., DAOD 2D distribution)
363 in the region of interest (see details in section 5.2).

364 Based on the monthly mean size-resolved dust DREE datasets derived above, we further
365 calculate globally annual mean size-resolved dust DREE^{SW} and DREE^{LW} at TOA and surface for
366 the six dust models (Figure 5). As discussed above, the global mean dust DREEs depends on the
367 DAOD spatial distribution, the global mean dust DREEs shown in Figure 5 is based on CALIOP-

368 based DAOD spatial distribution from Song et al. (2021). Generally smaller bins cause stronger
 369 cooling in SW and less warming in LW, which is consistent with our discussions in 3.1. This
 370 observationally informed globally annual mean size-resolved dust DREE is also consistent with
 371 the model-simulated results shown in supplementary Figure S3 in Kok et al. (2017) in terms of the
 372 variation trend of DREE with respect to dust size. Moreover, our study explicitly shows the
 373 sensitivity of dust DREE to dust RI and dust shape. For example, Figure 5 shows that $DREE^{SW}$ is
 374 strongly sensitive to dust RI as $DREE^{SW}$ of different dust RI is widely separated. Depending on
 375 dust RI, $DREE^{SW}$ switches from cooling effect (negative value) to warming effect (positive value)
 376 at different size bins. More absorptive dust starts to warm the Earth system in SW at smaller dust
 377 size, and vice versa. In addition, our results suggest that $DREE^{SW}$ is generally not sensitive to dust
 378 shape. Specifically, dust shape is not important for $DREE^{SW}$ in most size bins, while it is important
 379 in the fourth size bin ($D: 0.79\mu m \sim 1.58\mu m$) with $DREE^{SW}$ of spheroidal dust obviously higher
 380 (less negative) than spherical dust. In the $DREE^{LW}$, dust shape is almost as important as RI for
 381 several size bins.



383 Figure 4. Schematic of the methodology used to derive size-resolved dust DREE dataset. Orange boxes denote dust
 384 models used to calculate dust scattering properties. Red boxes denote inputs for RRTM. Green boxes denote outputs
 385 from RRTM.



386

387 Figure 5. Globally annual mean size-resolved dust DREE in SW (a) and LW (b) for six dust models (six markers).
 388 Horizontal bars indicate the dust diameter range of each size bin. Note: LW DREE is on a logarithm scale; in contrast
 389 to global model simulations, we consider dust LW scattering in LW DRE Efficiency calculations.

390 Our size-resolved dust DREE dataset is unique in many aspects: First, our DREE dataset
 391 is derived based on CALIOP-based dust 3D distribution. Size-resolved DREE is derived for all
 392 grids with CALIOP-based DAOD ≥ 0.01 . Second, our size-resolved DREE dataset covers a wide
 393 range of dust diameters, specifically, they include dust DREE for ten dust diameter size bins
 394 ranging from $0.1 \mu\text{m}$ to $100 \mu\text{m}$. This is challenging, if not impossible, to obtain from global
 395 models because these models generally simulate dust particles with diameter only up to $20 \mu\text{m}$ and
 396 coarse dust particles in models deposit quickly and could not be sustained to the remote transport
 397 regions (Huneeus et al., 2011; Adebisi and Kok, 2020) where coarse particles have been observed
 398 by in-situ measurements (Weinzierl et al., 2017). As a result, our size-resolved DREE dataset
 399 achieves a wide spatial coverage for a large range of dust size. This is critical for investigating
 400 impacts of coarse dust and even giant dust particles on dust DRE on both regional and global scales.
 401 Third, considering that the dust vertical distribution is important for quantifying DRE^{LW} , we
 402 constrain dust vertical distribution using CALIOP-based dust retrievals in DRE^{LW} computation.
 403 Fourth, our size-resolved dust DREE dataset accounts for dust LW scattering in DRE^{LW}
 404 calculations since scattering capability is available through the DISORT in RRTM_LW (Stamnes

405 et al., 1988). Dufresne et al., (2002) suggests that dust LW scattering enhances dust LW warming
406 effect at TOA by a factor of up to 50%. However, dust LW scattering is generally not considered
407 in most global models. Therefore, many previous studies artificially account for dust LW scattering
408 by increasing the radiative perturbation due to LW absorption by a certain fraction. For example,
409 Kok et al. (2017) accounts for LW scattering by artificially augmenting DRE^{LW} by 23% and Di
410 Biagio et al. (2020) augmented DRE^{LW} by 50%.

411 On the other hand, our size-resolved dust DREE dataset has several limitations. First,
412 possible vertical and horizontal variations of dust particle size in each grid box ($5^\circ \times 2^\circ$) are not
413 accounted for in our calculation. The entire dust-loading column in each grid box is assumed to
414 have the same dust size distribution. Second, we do not explicitly account for spatial variation of
415 dust RI, in other words, dust RI is assumed to be globally uniform. This uncertainty is assessed
416 through the sensitivity tests of DREE to dust RI using three sets of state-of-the-art dust RI based
417 on laboratory measurement of 19 dust samples all over the world. Third, dust 3D distribution in
418 the DREE calculation is constrained by CALIOP observations. The limits on the sensitivity of
419 CALIOP will affect the 3D distribution of dust in our calculation. Fourth, we account for dust
420 nonsphericity by using spheroidal shape model. This shape can't perfectly represent the highly
421 irregular shape and roughness of real dust. In addition, several studies suggest that dust non-
422 sphericity is underestimated by the spheroidal shape model (Huang et al., 2020). The spheroidal
423 shape model assumption thus might produce systematic errors.

424 Overall, the size-resolved dust DREE dataset is useful in many dust-related studies. First,
425 with our size-resolved dust DREE dataset, dust DRE could be calculated efficiently for any DAOD
426 magnitude, DAOD spatial pattern and any dust PSD for any regions or the globe (see details in
427 Section 4.1). Second, our size-resolved DREE dataset is derived for different RI and different dust

428 shapes respectively. As a result, we could estimate dust DRE uncertainty coming from DAOD,
 429 PSD, RI, and shape separately to better understand major uncertainty sources in dust DRE
 430 estimations. Third, our size-resolved DREE dataset could be used to evaluate model simulated
 431 DREE for each size bin.

432 **4 DRE calculation methodology and its validation**

433 **4.1 DRE calculation based on DREE dataset**

434 With the size-resolved dust DREE dataset derived in section 3.2, DRE of dust with any
 435 PSD and DAOD could be computed very efficiently without performing radiative transfer
 436 simulations as we do in *conventional* method. This section introduces the methodology of applying
 437 the size-resolved DREE dataset to calculate DRE of dust with any PSD and DAOD.

438 DRE of full-size range of dust can be expressed as the sum of DRE from each size bin
 439 (DRE_k). Dust DRE_k is approximated to be linearly proportional to DAOD of k^{th} size bin ($DAOD_k$)
 440 (Satheesh and Ramanathan, 2000). The similar concept of calculating dust DRE has been used in
 441 previous studies e.g., Kok et al. (2017). Eq. (6) shows the process of computing dust DRE using
 442 the size-resolved DREE dataset.

$$DRE = \sum_k DRE_k = \sum_k DREE_k \times DAOD_k = \sum_k DREE_k \times f_k \times DAOD, \quad (6)$$

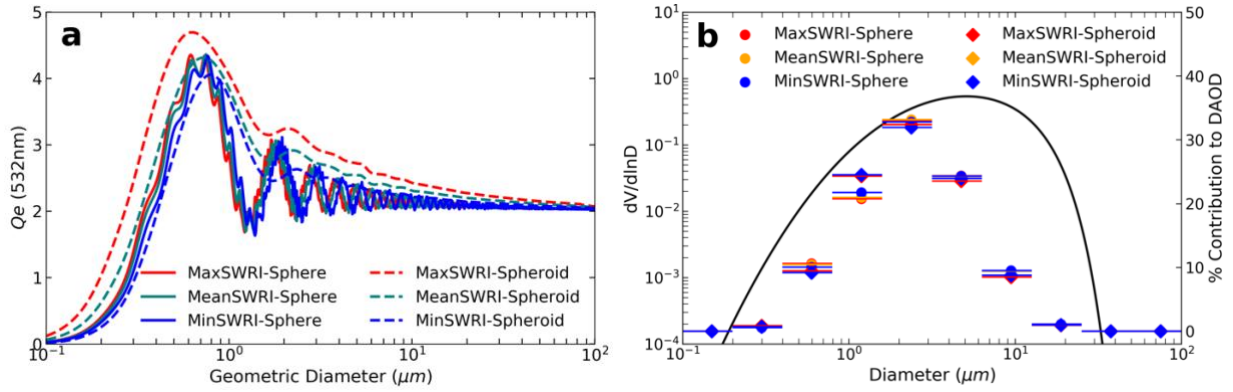
443 where DRE represents dust DRE induced by full size range of dust with optical depth of $DAOD$.
 444 f_k is the fraction of the DAOD contributed by the k^{th} size bin.

445 Each variable in Eq. (6) can be obtained or derived from datasets developed in this study
 446 and other studies. For example, the size-resolved DREE dataset ($DREE_{k,i,j}$) derived in this study
 447 is essential for utilizing this efficient and novel DRE calculation method. DAOD can be obtained
 448 from CALIOP-based or MODIS-based DAOD climatological datasets (Song et al., 2021). f_k can

449 be derived from dust extinction efficiency (Qe), the geometric cross-sectional area (A) and dust
 450 PSD (dN/dD) based on Eq. (7).

$$f_k \equiv \frac{DAOD_k}{DAOD} = \frac{\int_{D^{k-}}^{D^{k+}} Qe^{532nm}(D)A(D) \frac{dN}{dD} dD}{\int_0^{D^{max}} Qe^{532nm}(D)A(D) \frac{dN}{dD} dD} \quad (7)$$

451 Qe is defined according to $Qe \equiv \frac{\sigma_e}{A}$, where σ_e is extinction cross section, the geometric
 452 cross-sectional area of the particle (A) can be expressed as $A = \pi r^2$. Under the assumption of
 453 spherical dust particle, r is the radius. Under the assumption of spheroidal dust particle, Vouk
 454 (1948) shows that the average projected area of a convex body (e.g., spheroidal particle) is $A =$
 455 πr^2 , where r is the radius of a surface area-equivalent sphere. The average is taken over all
 456 possible orientations in space, which is consistent with our assumption of randomly oriented dust
 457 particles in the atmosphere. $Qe^{532nm}(D)$ for the six dust models are shown in Figure 6 (a), they
 458 all converge to 2 as the dust diameter becomes much larger than the wavelength, which is
 459 consistent with the principle of geometric optics (van de Hulst, 1957). By contrast, $Qe^{550nm}(D)$ of
 460 non-spherical dust in Kok et al. (2017) has a much larger value than spherical dust for dust $D \geq$
 461 $1\mu m$ (see their Figure 1(b)). This discrepancy is probably due to the different Qe definitions used
 462 in the two studies. Kok et al. (2017) defined Qe as dust extinction per unit cross section of volume-
 463 equivalent sphere. Figure 6 (b) shows that f_k of a specific PSD is not sensitive to dust RI and dust
 464 shape, this is also suggested by the similar Qe^{532nm} v.s. geometric diameter (D) trends of the six
 465 dust models shown in Figure 6 (a). In contrast, f_4 (i.e., f_k for the fourth size bin with D ranging
 466 from $0.79\mu m$ to $1.58\mu m$) is more sensitive to dust shape than other size bins, this is in line with
 467 the larger difference in Qe^{532nm} with shape shown in Figure 6 (a).



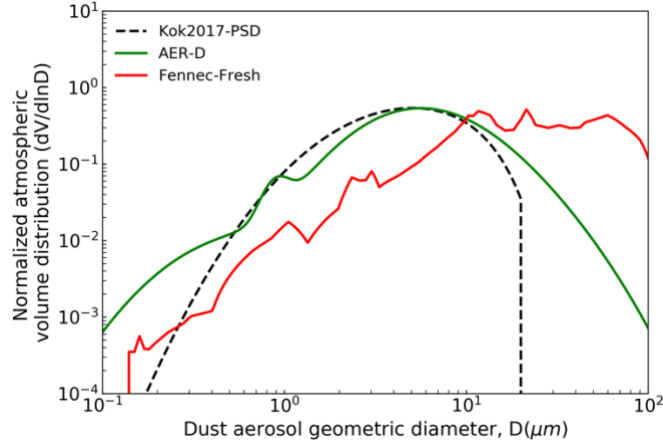
468

469 Figure 6. (a) Dust extinction efficiency (Q_e) at 532nm for six dust models. (b) The colorful bars represent f_k
 470 calculated for six dust models based on a specific dust PSD ($dV/d\ln D$) indicated by black curve. Note, f_k is not
 471 sensitive to different dust models such as dust RI and dust shape.

472 In summary, the size-resolved dust DREE dataset provides an efficient way to compute
 473 DRE for any dust PSD and any DAOD by using Eq. (6) and Eq. (7). To distinguish from the
 474 *conventional* method introduced in section 3.2, this method of calculating dust DRE based on size-
 475 resolved DREE dataset is referred to as ‘*DREE-integration*’ method.

476 4.2 Validation of DRE calculation methodology

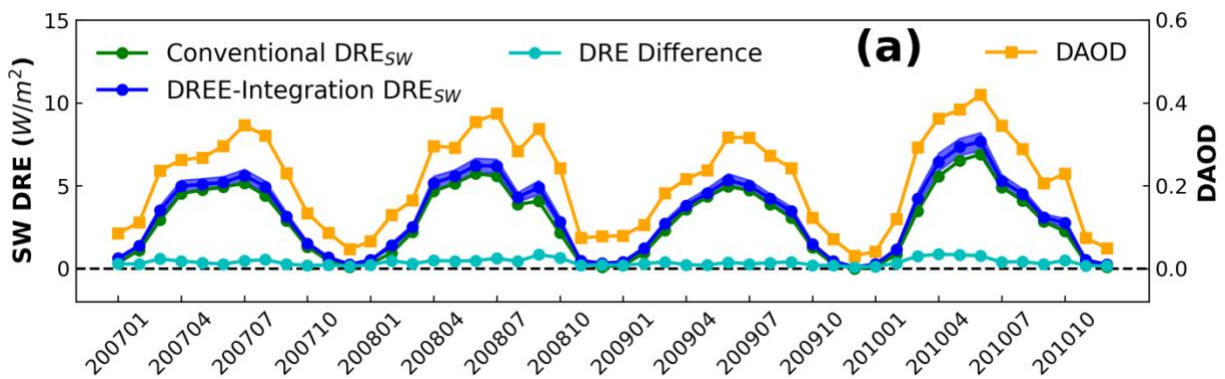
477 In this section, we select the Sahara Desert (14°N - 30°N , 15°W - 30°E) to validate the
 478 *DREE-integration* method. We choose MeanSWRI-MeanLWRI-Spheroid dust model and Fennec-
 479 Fresh dust PSD (see red curve in Figure 7) measured within 12h of dust uplift in remote Sahara
 480 locations by Fennec field campaign to represent microphysical properties of Saharan dust (Ryder
 481 et al., 2013a, b). Monthly mean DAOD is from CALIOP-based DAOD climatology.



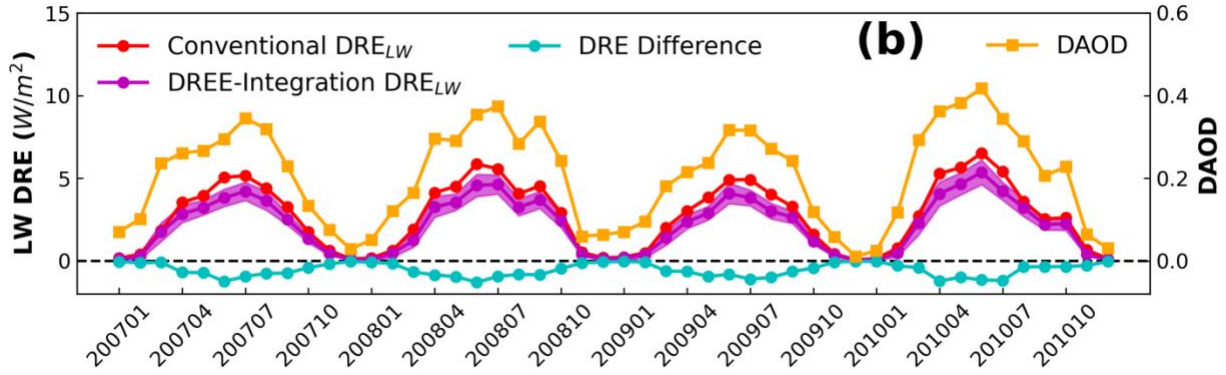
482

483 Figure 7. Normalized atmospheric dust volume distribution ($dV/d\ln D$) described in Table 5 (Kok et al., 2017; Ryder
484 et al., 2013a; b; 2018; 2019).

485 Figure 8 shows the comparison of 4-year (2007-2010) monthly mean dust DRE between
486 the *Conventional* and *DREE-integration* method. In Conventional DRE calculation, dust scattering
487 properties (Q_e , ω and g) are calculated based on the Fennec-Fresh PSD and then used to calculate
488 monthly mean dust DRE from 2007 to 2010 with RRTM as described in Section 3.2 (Eq. 1 – Eq.
489 4). While the DREE-integration method is based on the monthly mean size-resolved DREE dataset
490 derived based on 4-year (2007-2010) data as described in Section 4.1 (Eq. 6 – Eq. 7). The excellent
491 agreement in monthly mean dust DRE between two methods validates the *DREE-integration* DRE
492 calculation methodology.



493



494

495 Figure 8. Monthly mean dust DRE^{SW} (a) and DRE^{LW} (b) comparison between *Conventional* and *DREE-integration*
 496 calculation from 2007 to 2010 over Sahara Desert. The DRE Difference line represents the difference between *DREE-*
 497 *integration* and *Conventional* calculation. Shaded area along *DREE-integration* DRE indicates the one standard
 498 deviation caused by the atmospheric and surface variations as well as dust vertical distribution variation within the
 499 four years. Orange curves indicate CALIOP-based monthly mean DAOD. The variation of dust DRE match well with
 500 DAOD variation.

501 The shaded-area associated with DREE-integration DRE corresponds to the one standard

502 deviation of DREE caused by the 4-year (2007-2010) interannual variation of factors except dust

503 microphysical properties such as monthly mean atmospheric and surface properties as well as dust

504 vertical distributions (hereafter those factors is referred to as non-dust-factors for short). The

505 narrow shaded-area along DREE-integration DRE suggests non-dust-factors cause very small

506 uncertainty in dust DRE estimations. However, the small effects of 4-year interannual variation of

507 non-dust-factors may not necessarily be representative due to the limited number of years

508 considered. Section 2.1 discusses in detail for the reason of choosing 2007-2010 to derive size-

509 resolved DREE dataset. To check the representative of 4-year interannual variation for non-dust-

510 factors, we compare the 4-year (2007-2010) and 10-year (2007-2017) interannual standard

511 deviation (std) of monthly mean non-dust-factors (e.g., surface albedo, surface temperature and

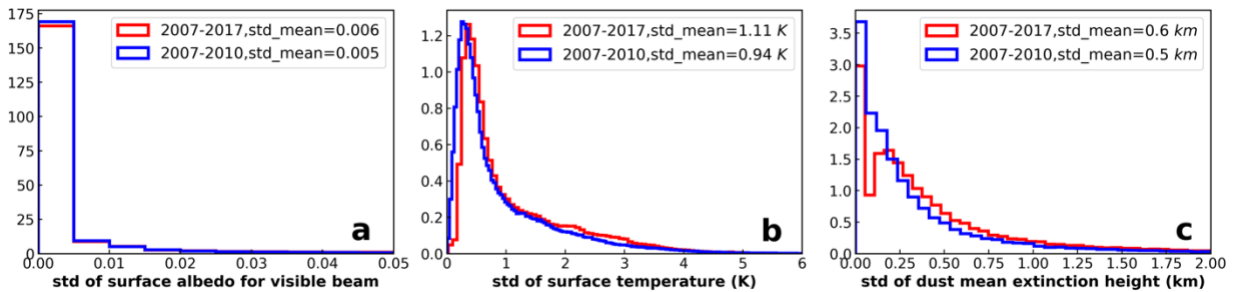
512 dust vertical distribution) in Figure 9. To evaluate the interannual variation of dust vertical

513 distribution, we define dust mean extinction height (Z_α) referring to Koffi et al. (2012) as $Z_\alpha =$

514 $\frac{\sum_{i=1}^n \beta_{ext,i} \times Z_i}{\sum_{i=1}^n \beta_{ext,i}}$, where $\beta_{ext,i}$ is the dust extinction coefficient at 532nm at level i , and Z_i is the altitude

515 of level i . Nevertheless the 10-year std is slightly larger than 4-year std, they are both close to zero

516 and on the same order of magnitude. As such, even though our monthly mean size-resolved DREE
 517 dataset is derived from 4-year (2007-2010) data, they could be used to represent DREE and
 518 calculate DRE for other years considering the small sensitivity of monthly mean dust DRE to
 519 interannual variation of non-dust-factors.



520
 521 Figure 9. Probability density function (PDF) of 4-year and 10-year interannual standard deviation (std) in monthly
 522 mean (a) surface albedo, (b) surface temperature, and (c) dust mean extinction height. The PSD analyses include
 523 interannual std in 12 months and all 5° (longitude) \times 2° (latitude) grid cells over the world and their mean values are
 524 indicated as 'std_mean' on each figure.

525 5 Regional and global dust DRE based on size-resolved DREE dataset

526 After the validation of *DREE-integration* method in Section 4, we use the *DREE-integration*
 527 method to calculate regional and global dust DRE in this section. There are three main objectives
 528 in this section: (1) the most important objective throughout this section is to demonstrate the
 529 usefulness of the size-resolved DREE dataset for calculating regional and global dust DRE for any
 530 given dust PSD; (2) the second objective is to validate the size-resolved DREE dataset by
 531 comparing with regional dust DREE reported by field studies based on satellite and ground-based
 532 observations (section 5.1); (3) the third objective to assess the sensitivity of dust DRE to DAOD
 533 spatial pattern (section 5.2) as well as dust microphysical properties such as dust PSD, RI and
 534 shape (section 5.3).

535 5.1 Comparison with observation-based regional dust DREE

536 Table 3 shows the comparison of our calculations of clear-sky regional mean SW and LW
 537 DREE with those reported by field studies based on satellite and ground-based observations. We

538 first calculated regional mean dust DRE using the *DREE-integration* method, then divided by the
539 corresponding regional mean DAOD to get regional mean DREE, and then compared this with
540 observation-based results from previous studies. Comparing DREE allows eliminating differences
541 due to the variation in regional dust loading, optically represented by DAOD.

542 Knowledge of regional dust PSD is necessary for estimating dust DRE regionally. There are
543 several in-situ measurements of dust PSD over Sahara and tropical eastern Atlantic. The state-of-
544 the art airborne observations of Saharan dust from the Fennec field campaign (Fennec-Fresh) and
545 transported Saharan dust over tropical eastern Atlantic within Saharan Air Layer (SAL) from both
546 AER-D and Fennec fieldwork campaigns are adopted (Ryder et al., 2013 a, b, 2018, 2019) (see
547 Figure 7). Both campaigns include giant dust particles, measuring up to $100\mu m$ diameter for AER-
548 D and up to $300\mu m$ for Fennec. The wide coverage of dust diameter in our size-resolved DREE
549 dataset allows for dust DRE calculations for giant dust up to $100\mu m$ over both dust source and
550 transported regions where giant particles are observed in those campaigns. This is an advantage of
551 our size-resolved DREE dataset compared to modeled dust DREE, because climate models
552 generally cut off dust diameter at $20\mu m$ and could not sustain coarse dust to remote transport
553 regions due to several missing mechanisms in models (Van Der Does et al., 2018; Drakaki et al.,
554 2022; Meng et al., 2022).

555 The Fennec-Fresh dust PSD includes measurements within 12h of dust uplift in remote
556 Sahara locations. It is used to calculate dust DRE for Saharan dust in this section. In reality, dust
557 over the wide Sahara Desert region ($15N\sim 30N$, $10W\sim 30E$) is not all lifted within 12h, so using
558 Fennec-Fresh to represent dust PSD over the wide Sahara Desert could bias dust size coarse, which
559 could partially explain the warm bias in our $DREE^{SW}$ estimation over the Sahara Desert compared
560 to the satellite-based result. Over the tropical Atlantic, both AER-D and Fennec-SAL measured

561 PSD are used to assess the sensitivity of dust DREE to dust PSD. In addition, dust DRE is
562 calculated for three dust RIs to evaluate the sensitivity of dust DREE to dust RI as shown in Table
563 3. Generally, our dust DREE estimations achieve good agreement with observation-based dust
564 DREE. However, there is a significant uncertainty caused by dust RI in DREE, especially for SW.
565 In addition, DRE comparisons between AER-D and Fennec-SAL over the Tropical Atlantic
566 suggests that in-situ measured dust PSD uncertainty leads to a large uncertainty in regional DREE
567 in both SW and LW.

568 Based on the regional DREE study with the state-of-the art RI and PSD, we found DREE^{SW}
569 uncertainty could come from both dust RI and dust PSD, while DRE^{LW} uncertainty is mainly from
570 dust PSD.

571 Table 3. Comparison of our DREE estimations for different PSD and RI with Clear-Sky regional SW and LW dust
572 DREE reported by field studies based on satellite and ground-based observations. Specifically, we calculated regional
573 dust DREE for different RI (Min, Mean, Max) and different PSD (AER-D and Fennec-SAL for Tropical Atlantic) and
574 then compare with observation-based results from previous studies. Note, spheroidal dust shape is assumed in our
575 DREE-integration DRE calculations.

Shortwave Spectral Range							
Region	Season	Level	Satellite- Based DREE ^{SW}	This study			
				DREE ^{SW}			PSD
				Min RI	Mean RI	Max RI	
Sahara Desert ^(a) (15N~30N, 10W~30E)	JJA	TOA	0	2.8	16.0	26.6	Fennec-Fresh
Ilorin ^(f) , Nigeria (8.5N, 4.7E)	Annual	TOA	-15 ~ -35	-28.3	-24.1	-19.9	AER-D
				-23.4	-17.7	-12.9	Fennec-SAL
		Surface	-49 ~ -75	-43.1	-51.7	-59.3	AER-D
				-46.0	-57.1	-66.0	Fennec-SAL
Cape Verde ^(f) (16.7N, 22.9W)	Annual	TOA	-36 ~ -48	-42.3	-38.0	-33.7	AER-D
				-36.6	-30.8	-26.0	Fennec-SAL
		Surface	-68 ~ -90	-59.6	-68.7	-77.7	AER-D
				-61.5	-74.6	-85.3	Fennec-SAL
Tropical Atlantic ^(b) (10N~30N, 20W~45W)	JJA	TOA	-28	-44.6	-39.9	-35.3	AER-D
				-38.4	-32.1	-27.0	Fennec-SAL
		Surface	-82.1	-61.1	-71.9	-81.7	AER-D
				-64.4	-78.5	-90.0	Fennec-SAL
Tropical Atlantic ^(c) (15N~25N, 15W~45W)	JJA	TOA	-35	-41.2	-36.3	-31.5	AER-D
				-35.1	-28.5	-23.1	Fennec-SAL
		Surface	-65	-57.9	-68.6	-78.1	AER-D
				-61.2	-75.1	-86.3	Fennec-SAL
Longwave Spectral Range							

Region	Season	Level	Satellite-Based DREE ^{LW}	This study			PSD
				Min RI	Mean RI	Max RI	
Sahara Desert ^(a) (15N~30N, 10W~30E)	JJA	TOA	11~26	13.4	11.8	11.4	Fennec-Fresh
North Africa ^(d-e) (15N~35N, 18W~40E)	JJA	TOA	15~22	14.4	12.8	12.4	Fennec-Fresh
Tropical Atlantic ^(b) (10N~30N, 20W~45W)	JJA	TOA	10.5	8.2	8.1	8.5	AER-D
				13.1	11.8	11.6	Fennec-SAL
Cape Verde ^(g) (16.7N, 22.9W)	Sept	Surface	16	8.0	11.8	15.1	AER-D
				13.0	17.0	19.8	Fennec-SAL

(a) Patadia et al. (2009). (b) Song et al. (2018). (c) Li et al. (2004). (d) Zhang and Christopher (2003). (e) Brindley and Russell (2009). (f) Zhou et al. (2005). (g) Hansell et al. (2010)

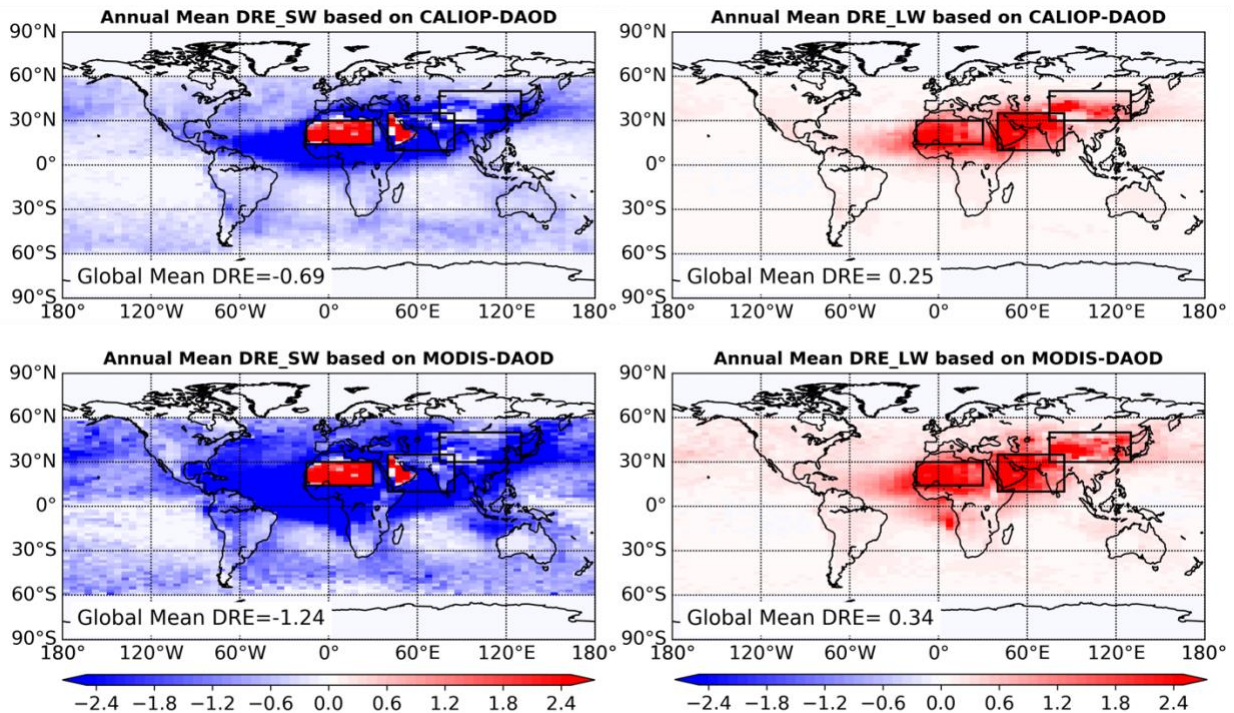
576

577 5.2 Global dust clear-sky DRE based on different DAOD climatology

578 The DAOD is the most important factor in determining dust DRE. As illustrated in Song et
579 al. (2021), the DAOD retrieved from different satellite sensors have a large difference in terms of
580 magnitude and spatial distribution. To evaluate how the current DAOD uncertainty affects dust
581 DRE estimations, the global dust DRE computed based on monthly mean DAOD climatology
582 retrieved from CALIOP observations and MODIS observations are compared in this section. To
583 separate the effect of DAOD from other factors, we use the same dust PSD, RI and shape in the
584 two sets of dust DRE calculations in this section. Specifically, we use the Fennec-Fresh PSD for
585 three major dust source regions (i.e., Sahara (14-30°N, 15°W-30°E), Middle East (10-35°N, 40-
586 85°E) and eastern Asia (30-50°N, 75-130°E), they are indicated by three black boxes in Figure 10)
587 and use AER-D PSD for other regions (hereafter Campaign-PSD, see Table 5). The MeanSWRI-
588 MeanLWRI-Spheroid dust model described in Table 1 is used to represent dust RI and shape.

589 The two DAOD climatological datasets result in distinct dust DRE spatial pattern as shown
590 in Figure 10, which is consistent with the DAOD spatial patterns shown in Figure 1 suggesting
591 CALIOP DAOD is more concentrated over ‘dust belt’ regions than MODIS DAOD. The global
592 mean dust DRE^{SW}, DRE^{LW} and DRE^{NET} based on the two DAOD climatology are significantly

593 different (Table 4), which is mainly caused by two factors. The first is the difference in DAOD
 594 magnitude. The CALIOP-based global mean DAOD is 0.032, while MODIS-based is 0.047. The
 595 other factor is the difference in DAOD spatial pattern. After we scale dust DRE to the same global
 596 mean DAOD ($\overline{DAOD} = 0.03$) to eliminate the effect of DAOD magnitude difference (values in
 597 parentheses in Table 4), the DRE^{SW} difference reduced from 0.55 W m^{-2} (-0.69 vs. -1.24 W m^{-2})
 598 to 0.15 W m^{-2} (-0.64 vs. -0.79 W m^{-2}). Similarly, differences in DRE^{LW} and DRE^{NET} also reduce
 599 significantly. It indicates that the global mean DAOD magnitude difference is more important than
 600 the subtle difference in spatial pattern. Nevertheless, after scaling to the same global mean DAOD
 601 there is still more than 10% difference between the two dust DRE^{SW} , with CALIOP-based being
 602 the more positive one. This is probably because CALIOP-based DAOD is more concentrated over
 603 dust sources where dust aerosols induce less negative or even positive DRE^{SW} (For example the
 604 positive DRE^{SW} over the Sahara Desert and Arabia shown in Figure 10), which result in a less
 605 negative global mean DRE^{SW} than MODIS.



606

607 Figure 10. Annual mean dust DRE global distribution based on CALIOP-based and MODIS-based DAOD
 608 climatology. MeanSWRI-MeanLWRI-Spheroid dust model are used to represent dust RI and shape in the calculation.
 609 Campaign-PSD is used to represent dust PSD, specifically, Fennec-Fresh PSD is used to represent dust PSD over the
 610 three major dust source regions indicated by three black boxes. AER-D PSD is used to represent dust PSD over other
 611 regions.

612 Table 4. Globally annual mean DAOD, DRE^{SW} , DRE^{LW} and DRE^{NET} based on CALIOP DAOD and MODIS DAOD
 613 climatology. Note, values in the parentheses are for the two DAOD scaled to the same value of 0.03.

	\overline{DAOD}	$\overline{DRE^{SW}}$ [Wm^{-2}]	$\overline{DRE^{LW}}$ [Wm^{-2}]	$\overline{DRE^{NET}}$ [Wm^{-2}]
CALIOP	0.032 (0.03)	-0.69 (-0.64)	0.25 (0.23)	-0.44 (-0.41)
MODIS	0.047 (0.03)	-1.24 (-0.79)	0.34 (0.22)	-0.90 (-0.57)

614

615 5.3 Global dust clear-sky DRE based on different dust PSD

616 In the section 5.2, we showed the dust DRE based on the Campaign-PSD. As aforementioned,
 617 one of the main advantages of our size-resolved DREE is that it can be combined with different
 618 dust PSDs to estimate the dust DRE. To demonstrate this, we calculate another set of dust DRE
 619 based on the Kok2017-PSD. Table 5 describes the two dust PSDs used for global dust DRE
 620 calculations and their references. Kok2017-PSD is a globally averaged dust PSD and used to
 621 represent dust PSD for each dusty grid cell. It is constrained with observations and includes coarse
 622 dust particles up to $20\mu m$. Although our primary goal here is to demonstrate the capability of our
 623 size-resolved DREE, the comparison between the two DRE can also help us understand the
 624 impacts of dust PSD uncertainty on the dust DRE estimation. Moreover, we also investigate the
 625 sensitivity of DRE to dust RI and dust shape explicitly in this section. The same DAOD
 626 climatology (CALIOP-based DAOD climatology) is used for dust DRE calculations to eliminate
 627 the impact of dust loading difference.

628 Several recent observation-constrained dust PSDs (e.g., Di Biagio et al., 2020, Adebisi et
 629 al., 2020) suggest that dust size is coarser than Kok2017-PSD. As such, Kok2017-PSD is used to
 630 represent the lower limit of the observation-based global dust PSD to investigate the sensitivity of
 631 dust DRE to dust PSD. The Campaign-PSD is purely based on aircraft in-situ measurements and

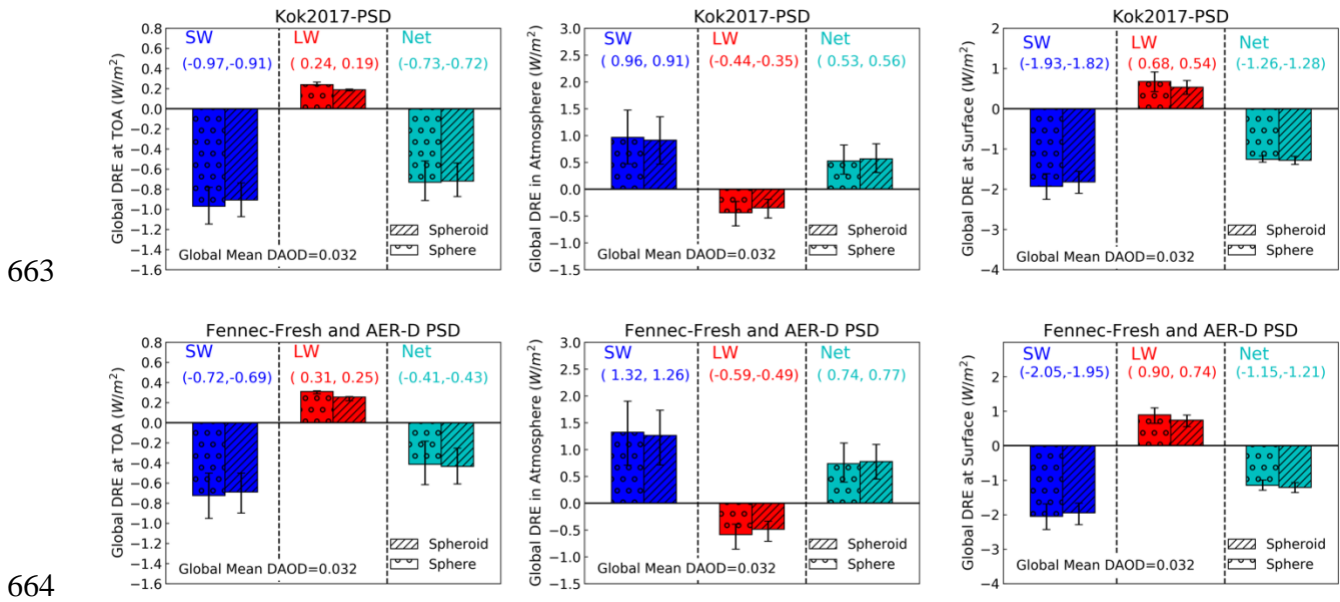
632 the aircraft was extensively equipped to measure giant particles with diameter larger than $20\mu m$.
633 We use the dust PSD measured over Sahara (from the Fennec field campaign) to represent dust
634 PSD over three major dust source regions and use dust PSD measured in the Saharan Air Layer
635 over the tropical eastern Atlantic (from AER-D field campaign) to represent dust PSD over dust
636 transport regions. Of course, representing the spatial and temporal variation of global dust PSD
637 with only two PSDs from the field campaigns is only a crude approximation due to the lack of
638 PSD measurements. Dust aerosol over the three wide dust source regions may not be all uplifted
639 within 12 hours as in the Fennec-Fresh measurements, in addition, dust size after long-range
640 transport could be a bit finer than dust PSD measured over tropical eastern Atlantic (Weinzierl et
641 al., 2017). Thus, Campaign-PSD likely represents the upper limit of the observation-based global
642 dust PSD for the investigation of sensitivity to dust PSD. By contrast, the climate models miss
643 most of coarse dust ($D > 5\mu m$) in the atmosphere (Adebiyi and Kok, 2020), as a result, the purely
644 modeled dust PSD without observational constraints will lead to a substantially different dust DRE.
645 Therefore, the sensitivity test to dust PSD conducted in this study can only represent the
646 uncertainty induced by the current understanding of observation-based dust PSD.

647 Table 5. The two observation-based dust PSDs used in DRE calculations (see Figure 7).

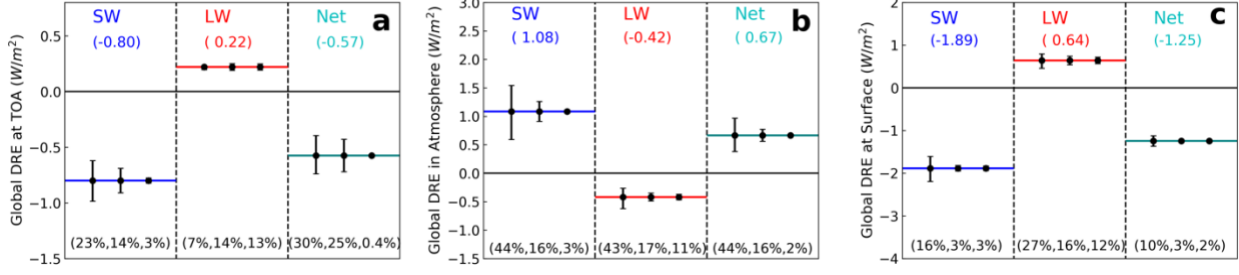
PSD	Description	Reference
Kok2017-PSD	A globally averaged atmospheric PSD derived from observation constrained globally averaged emitted PSD and model simulated globally averaged dust lifetime. This globally averaged PSD is used to represent dust PSD for each dusty grid cell. Dust diameter is cutoff at $20\mu m$ (Figure 2a in Kok et al.2017).	Kok et al. (2017)
Campaign-PSD	Fennec-Fresh PSD is used for three major dust source regions (i.e., Sahara (14-30°N, 15°W-30°E), Middle East (10-35°N, 40-85°E) and eastern Asia (30-50°N, 75-130°E)), which are indicated by the three black boxes in Figure 10. AER-D PSD is used for other regions.	Ryder et al. (2013a, b, 2018, 2019)

648
649 We calculated dust DRE of each grid cell ($DRE_{i,j}$) using *DREE-integration* method based
650 on the dust PSD described in Table 5. Global mean dust DRE was then calculated by averaging

651 dust $DRE_{i,j}$ weighted by its surface area. Figure 11 shows the global mean DRE^{SW} , DRE^{LW} and
 652 DRE^{NET} at TOA, surface, and in the atmosphere calculated based on the two sets of PSDs.
 653 Obviously, Kok2017-PSD leads to stronger cooling effect in SW and weaker warming effect in
 654 LW at TOA compared to Campaign-PSD, which is consistent with the fact that Kok2017-PSD is
 655 finer than the Campaign-PSD. In addition, we explicitly include the effects of dust RI and dust
 656 shape on DRE in Figure 11. Comparison of uncertainty induced by dust PSD, RI and shape
 657 suggests that dust RI uncertainty leads to the largest uncertainty in dust DRE, particularly RI
 658 uncertainty induces more than 40% uncertainty in DRE^{SW} estimations in the atmosphere (Figure
 659 12). Dust PSD is also important for quantifying dust DRE, we found that the observation-based
 660 dust PSD uncertainty induces around 15%~20% uncertainty in dust DRE at TOA and in the
 661 atmosphere. Dust non-sphericity causes a negligible uncertainty in global mean dust DRE, in line
 662 with previous studies e.g., Raisanen et al. (2013) and Colarco et al. (2014).



665 Figure 11. Globally annual mean clear-sky DRE^{SW} , DRE^{LW} and DRE^{NET} at TOA, in the atmosphere and surface
 666 calculated based on the two PSDs described in Table 5. The two rows represent dust DRE based on two PSDs.
 667 Error bars indicate uncertainty induced by dust RI uncertainty. Different types of bars indicate dust DRE based on different
 668 dust shapes. This figure explicitly separates the impacts of different dust microphysical properties on dust DRE. Two
 669 values in parenthesis on each plot represent spherical (left) and spheroidal (right) dust DRE corresponding to mean
 670 RI.



671

672 Figure 12. Comparison of uncertainty induced by dust RI, PSD and shape in DRE^{SW} , DRE^{LW} and DRE^{NET} at TOA (a),
 673 in the atmosphere (b) and surface (c). The horizontal lines in each plot represent global mean DRE^{SW} (blue line in the
 674 left column), DRE^{LW} (red line in the middle column) and DRE^{NET} (green line in the right column) averaged over two
 675 dust PSDs (i.e., Kok2017-PSD and Campaign-PSD) based on MeanRI-Spheroid dust model. The three error bars in
 676 each column represent DRE uncertainty induced by dust RI (left), dust PSD (middle) and dust shape (right).
 677 Accordingly, the percentage values on the bottom represent the percentage uncertainty induced by dust RI, PSD and
 678 shape, respectively.

679 It is tempting to compare our global mean dust DRE with results reported in Kok et al. (2017).

680 But it must be noted that the global mean dust DRE shown in Figure 11 is for *clear sky* only, while

681 the global mean dust DRE reported in Kok et al. (2017) is for *all sky*. The all-sky dust DRE can

682 be separated into contributions from clear-sky and cloudy-sky portions (Myhre et al., 2020):

$$DRE_{all-sky} = (1 - CF) \times DRE_{clear-sky} + CF \times DRE_{cloudy-sky}, \quad (8)$$

683 where CF is cloud fraction, $DRE_{clear-sky}$ is dust DRE simulated under the case of removing all

684 clouds, $DRE_{cloudy-sky}$ is the dust DRE assuming whole grid is covered by clouds. To compare

685 our global mean dust DRE^{SW} based on Kok2017-PSD with the results reported in Kok et al. (2017),

686 we convert our clear-sky $DRE_{clear-sky}^{SW}$ to $DRE_{all-sky}^{SW}$ by using MODIS L3 monthly mean cloud

687 fraction. Specifically, we multiply $DRE_{clear-sky}^{SW}$ by $(1-CF)$ for each grid cell and then calculate

688 global annual mean values. In this process, we neglect the cloudy-sky dust DRE^{SW} portion because

689 the annual mean cloudy-sky dust DRE^{SW} is estimated to be very small, around -0.04 (Zhang et

690 al., 2016). Finally, our estimated global mean $DRE_{all-sky}^{SW}$ corresponding to DAOD=0.03 is around

691 $-0.34 Wm^{-2}$. Although it is comparable to the $-0.48 Wm^{-2}$ from Kok et al. 2017, the following

692 differences between the two studies must be kept in mind when interpreting the results. First, the

693 rough conversion from global mean $DRE_{clear-sky}^{SW}$ to global mean $DRE_{all-sky}^{SW}$ is subject to the
694 approximation of global mean $DRE_{cloudy-sky} \sim 0$ and the MODIS L3 cloud fraction could be
695 different from modeled cloud fraction used in Kok et al. (2017). Second, the two studies use
696 different dust RI. For example, the imaginary part of RI at 550nm in this study ranges from 0.00061
697 to 0.003, while that in Kok et al. (2017) ranges from 0.0014 as used in GEOS-Chem and GISS
698 model based on Sinyuk et al., (2003) to 0.003 as used in WRF-Chem based on Zhao et al., (2010).
699 Third, in this study Kok2017-PSD is used to represent dust PSD in each dusty grid and applied to
700 our size-resolved dust DREE dataset to calculate global dust DRE. In contrast, the model-
701 simulated dust DREE in Kok et al. (2017) has reduced cooling from SW scattering and enhanced
702 warming from SW absorption effects because the short lifetime of coarse dust in models
703 concentrates these particles over bright deserts. Fourth, the two studies use different dust shape
704 models, Kok et al. (2017) accounts for more nonspherical shape model (i.e., tri-axial ellipsoids).
705 Here we do not compare our global mean $DRE_{clear-sky}^{LW}$ with $DRE_{all-sky}^{LW}$ suggested in Kok et al.
706 (2017) because that the lack of knowledge in $DRE_{cloudy-sky}^{LW}$ prevent us to convert $DRE_{clear-sky}^{LW}$
707 to $DRE_{all-sky}^{LW}$. Moreover, the two studies use different dust vertical profile, which is critical for
708 DRE^{LW} estimations. For instance, dust vertical profile in Kok et al. (2017) is purely based on model
709 simulations, while this study constrains dust vertical profile with CALIOP observations.
710 Considering all these factors, it is hard to tell if the comparison is fair.

711 **6 Summary and Conclusion**

712 This study developed a clear-sky size-resolved dust DREE dataset in both SW and LW
713 based on CALIOP-based dust DAOD climatology and dust vertical distributions. The dataset
714 contains global monthly mean dust DREE at TOA and surface with 5° (longitude) \times 2° (latitude)

715 spatial resolution for 10 size bins ranging from $0.1\mu\text{m}$ to $100\mu\text{m}$ diameter, for three state-of-the
716 art dust RI representing more, mean and less absorptive dust, and for two dust shapes representing
717 spherical and spheroidal dust, respectively.

718 The size-resolved DREE dataset allows us to calculate dust DRE of any DAOD
719 climatology and dust PSD efficiently by using the *DREE-integration* method presented in section
720 4.1 without involving radiative transfer simulations. The *DREE-integration* method is proven to
721 be in great agreement with *conventional* DRE calculations. With the *DREE-integration*
722 methodology, we firstly calculated clear-sky regional mean DREE^{SW} and DREE^{LW} over the Sahara
723 Desert and tropical Atlantic. The comparison of our calculations with those reported by field
724 studies based on satellite and ground-based observations shows reasonable agreement. Secondly,
725 we estimated global mean dust DRE with two satellite-based DAOD climatological datasets and
726 two different global dust PSDs. We found that the global mean DAOD magnitude difference
727 between the two DAOD climatological datasets is more important than the subtle difference in
728 spatial pattern. Nevertheless, after scaling to the same global mean DAOD there is still more than
729 10% difference between the two dust DRE^{SW} , with CALIOP-based being the more positive one.
730 Moreover, our results explicitly show the uncertainty induced by each dust microphysical property
731 (i.e., dust PSD, RI and shape) separately. When DAOD is constrained: (a) Dust non-sphericity
732 induces negligible effect on dust DRE estimations; (b) The current understanding of observation-
733 based dust PSD induces relatively large uncertainty (15%~20%) in dust DRE at TOA and in the
734 atmosphere (c) Dust RI turns out to be the most important factor in determining dust DRE,
735 particularly in SW. This implies that better understanding of dust mineral composition and RI will
736 significantly improve our understanding in dust DRE in the future.

737 *Data availability:*

738 The size-resolved dust DREE dataset and the codes to calculate dust DRE for any given
739 dust PSD and DAOD are available at

740 ‘https://drive.google.com/drive/folders/15_e28Y9JiSWiJnIM_2flEmt2u6i9phEY?usp=sharing’

741 CALIOP- and MODIS-based DAOD climatological datasets are available at

742 ‘<https://drive.google.com/drive/folders/1aQVupe7govPwR6qmsqUbr4fJQsp1DBCX?usp=sharing>
743 ng’

744

745 *Acknowledgement:*

746 We would like to thank Dr. Claire L. Ryder for providing the Fennec and AER-D dust
747 PSDs. Qianqian Song and Zhibo Zhang cordially acknowledge the funding support from the Future
748 Investigators in NASA Earth and Space Science and Technology (FINESST). Zhibo Zhang’s
749 research is supported by NASA grant (80NSSC20K0130) from the CALIPSO and CloudSat
750 program. S. Albani received funding from MIUR (Progetto Dipartimenti di Eccellenza 2018-2022).
751 The computations in this study were performed at the UMBC High Performance Computing
752 Facility (HPCF). The facility is supported by the US National Science Foundation through the
753 MRI program (grant nos. CNS-0821258 and CNS-1228778) and the SCREMS program (grant no.
754 DMS-0821311), with substantial support from UMBC.

755

756 References

- 757 Adebisi, A. A. and Kok, J. F.: Climate models miss most of the coarse dust in the
758 atmosphere, *Sci. Adv.*, 6, eaaz9507, <https://doi.org/10.1126/sciadv.aaz9507>, 2020.
- 759 Adebisi, A. A., Kok, J. F., Wang, Y., Ito, A., Ridley, D. A., Nabat, P., and Zhao, C.: Dust
760 Constraints from joint Observational-Modelling-experiMental analysis (DustCOMM):
761 Comparison with measurements and model simulations, *Atmos. Chem. Phys.*, 20, 829–863,
762 <https://doi.org/10.5194/acp-20-829-2020>, 2020.
- 763 Albrecht, B. A.: Aerosols, Cloud Microphysics, and Fractional Cloudiness, *Science (80-.)*,
764 245, 1227–1230, <https://doi.org/DOI.10.1126/science.245.4923.1227>, 1989.
- 765 Balkanski, Y., Schulz, M., Claquin, T., and Guibert, S.: Reevaluation of Mineral aerosol
766 radiative forcings suggests a better agreement with satellite and AERONET data, *Atmos. Chem.*
767 *Phys.*, 7, 81–95, <https://doi.org/10.5194/acp-7-81-2007>, 2007.
- 768 Di Biagio, C., Formenti, P., Balkanski, Y., Caponi, L., Cazaunau, M., Pangui, E., Journet,
769 E., Nowak, S., Caquaineau, S., Andreae O, M., Kandler, K., Saeed, T., Piketh, S., Seibert, D.,
770 Williams, E., and Doussin, J. F. C.: Global scale variability of the mineral dust long-wave
771 refractive index: A new dataset of in situ measurements for climate modeling and remote sensing,
772 *Atmos. Chem. Phys.*, 17, 1901–1929, <https://doi.org/10.5194/acp-17-1901-2017>, 2017.
- 773 Di Biagio, C., Formenti, P., Balkanski, Y., Caponi, L., Cazaunau, M., Pangui, E., Journet,
774 E., Nowak, S., Andreae, M. O., Kandler, K., Saeed, T., Piketh, S., Seibert, D., Williams, E., and
775 Doussin, J. F.: Complex refractive indices and single-scattering albedo of global dust aerosols in
776 the shortwave spectrum and relationship to size and iron content, *Atmos. Chem. Phys.*, 19, 15503–
777 15531, <https://doi.org/10.5194/acp-19-15503-2019>, 2019.
- 778 Di Biagio, C., Balkanski, Y., Albani, S., Boucher, O., and Formenti, P.: Direct Radiative
779 Effect by Mineral Dust Aerosols Constrained by New Microphysical and Spectral Optical Data,
780 *Geophys. Res. Lett.*, 47, e2019GL086186, <https://doi.org/doi:10.1029/2019GL086186>, 2020.
- 781 Brindley, H. E. and Russell, J. E.: An assessment of Saharan dust loading and the
782 corresponding cloud-free longwave direct radiative effect from geostationary satellite observations,
783 *J. Geophys. Res. Atmos.*, 114, <https://doi.org/10.1029/2008JD011635>, 2009.
- 784 Choobari, O. A., P. Zawar-Reza, and Sturman, A.: The global distribution of mineral dust
785 and its impacts on the climate system: A review, *Atmos. Res.*, 138, 152–165,
786 <https://doi.org/10.1016/j.atmosres.2013.11.007>, 2014.
- 787 Colarco, P. R., Nowotnick, E. P., Randles, C. A., Yi, B. Q., Yang, P., Kim, K. M., Smith,
788 J. A., and Bardeen, C. G.: Impact of radiatively interactive dust aerosols in the NASA GEOS-5
789 climate model: Sensitivity to dust particle shape and refractive index, *J. Geophys. Res.*, 119, 753–
790 786, <https://doi.org/10.1002/2013jd020046>, 2014.
- 791 Van Der Does, M., Knippertz, P., Zschenderlein, P., Harrison, R. G., and Stuut, J.-B. W.:
792 The mysterious long-range transport of giant mineral dust particles, *Sci. Adv.*, 4, 1–9, 2018.
- 793 Dubovik, O., Sinyuk, A., Lapyonok, T., Holben, B. N., Mishchenko, M., Yang, P., Eck, T.
794 F., Volten, H., Munoz, O., Veihermann, B., van der Zande, W. J., Leon, J. F., Sorokin, M., and
795 Slutsker, I.: Application of spheroid models to account for aerosol particle nonsphericity in remote
796 sensing of desert dust, *J. Geophys. Res.*, 111, <https://doi.org/Artn.D11208.10.1029/2005jd006619>,
797 2006.
- 798 Dufresne, J. L., Gautier, C., and Ricchiazzi, P.: Longwave scattering effects of mineral
799 aerosols, *J. Atmos. Sci.*, 59, 1959–1966, [https://doi.org/10.1175/1520-0469\(2002\)059<1959:LSEOMA>2.0.CO;2](https://doi.org/10.1175/1520-0469(2002)059<1959:LSEOMA>2.0.CO;2), 2002.

801 García, O. E., Díez, A. M., Expósito, F. J., Díaz, J. P., Dubovik, O., Dubuisson, P., Roger,
802 J. C., Eck, T. F., Sinyuk, A., Derimian, Y., Dutton, E. G., Schafer, J. S., Holben, B., and García,
803 C. A.: Validation of AERONET estimates of atmospheric solar fluxes and aerosol radiative forcing
804 by ground-based broadband measurements, *J. Geophys. Res. Atmos.*, 113,
805 <https://doi.org/10.1029/2008JD010211>, 2008.

806 Gelaro, R., McCarty, W., Suárez, M. J., Todling, R., Molod, A., Takacs, L., Randles, C.
807 A., Darmenov, A., Bosilovich, M. G., Reichle, R., Wargan, K., Coy, L., Cullather, R., Draper, C.,
808 Akella, S., Buchard, V., Conaty, A., da Silva, A. M., Gu, W., Kim, G. K., Koster, R., Lucchesi, R.,
809 Merkova, D., Nielsen, J. E., Partyka, G., Pawson, S., Putman, W., Rienecker, M., Schubert, S. D.,
810 Sienkiewicz, M., and Zhao, B.: The modern-era retrospective analysis for research and
811 applications, version 2 (MERRA-2), *J. Clim.*, 30, 5419–5454, [https://doi.org/10.1175/JCLI-D-16-](https://doi.org/10.1175/JCLI-D-16-0758.1)
812 [0758.1](https://doi.org/10.1175/JCLI-D-16-0758.1), 2017.

813 Ginoux, P., Prospero, J. M., Gill, T. E., Hsu, N. C., and Zhao, M.: Global-scale attribution
814 of anthropogenic and natural dust sources and their emission rates based on MODIS Deep Blue
815 aerosol products, <https://doi.org/10.1029/2012RG000388>, 1 September 2012.

816 Gkikas, A., Proestakis, E., Amiridis, V., Kazadzis, S., Di Tomaso, E., Tsekeri, A., Marinou,
817 E., Hatzianastassiou, N., and Pérez Garcíá-Pando, C.: ModIs Dust AeroSol (MIDAS): A global
818 fine-resolution dust optical depth data set, *Atmos. Meas. Tech.*, 14, 309–334,
819 <https://doi.org/10.5194/amt-14-309-2021>, 2021.

820 Hansell, R. A., Tsay, S. C., Ji, Q., Hsu, N. C., Jeong, M. J., Wang, S. H., Reid, J. S., Liou,
821 K. N., and Ou, S. C.: An assessment of the surface longwave direct radiative effect of airborne
822 Saharan dust during the NAMMA field campaign, *J. Atmos. Sci.*, 67, 1048–1065,
823 <https://doi.org/10.1175/2009JAS3257.1>, 2010.

824 Hsu, N. C., Jeong, M.-J., Bettenhausen, C., Sayer, A. M., Hansell, R., Seftor, C. S., Huang,
825 J., and Tsay, S.-C.: Enhanced Deep Blue aerosol retrieval algorithm: The second generation, *J.*
826 *Geophys. Res. Atmos.*, 118, 9296–9315, [https://doi.org/https://doi.org/10.1002/jgrd.50712](https://doi.org/10.1002/jgrd.50712), 2013.

827 Huang, Y., Kok, J. F., Kandler, K., Lindqvist, H., Nousiainen, T., Sakai, T., Adebisi, A.,
828 and Jokinen, O.: Climate Models and Remote Sensing Retrievals Neglect Substantial Desert Dust
829 Asphericity, *Geophys. Res. Lett.*, 47, <https://doi.org/10.1029/2019GL086592>, 2020.

830 van de Hulst, H. C.: *Light scattering by small particles*, Wiley, Hoboken, NJ, 1957.

831 Huneeus, N., Schulz, M., Balkanski, Y., Griesfeller, J., Prospero, J., Kinne, S., Bauer, S.,
832 Boucher, O., Chin, M., Dentener, F., Diehl, T., Easter, R., Fillmore, D., Ghan, S., Ginoux, P., Grini,
833 A., Horowitz, L., Koch, D., Krol, M. C., Landing, W., Liu, X., Mahowald, N., Miller, R., Morcrette,
834 J. J., Myhre, G., Penner, J., Perlwitz, J., Stier, P., Takemura, T., and Zender, C. S.: Global dust
835 model intercomparison in AeroCom phase i, *Atmos. Chem. Phys.*, 11, 7781–7816,
836 <https://doi.org/10.5194/acp-11-7781-2011>, 2011.

837 Kato, S., Rose, F. G., Sun-Mack, S., Miller, W. F., Chen, Y., Rutan, D. A., Stephens, G.
838 L., Loeb, N. G., Minnis, P., Wielicki, B. A., Winker, D. M., Charlock, T. P., Stackhouse, P. W.,
839 Xu, K. M., and Collins, W. D.: Improvements of top-of-atmosphere and surface irradiance
840 computations with CALIPSO-, CloudSat-, and MODIS-derived cloud and aerosol properties, *J.*
841 *Geophys. Res.*, 116, [https://doi.org/Artn D19209 10.1029/2011jd016050](https://doi.org/10.1029/2011jd016050), 2011.

842 Kaufman, Y. J., Koren, I., Remer, L. A., Tanré, D., Ginoux, P., and Fan, S.: Dust transport
843 and deposition observed from the Terra-Moderate Resolution Imaging Spectroradiometer
844 (MODIS) spacecraft over the Atlantic Ocean, *J. Geophys. Res. D Atmos.*, 110, 1–16,
845 <https://doi.org/10.1029/2003JD004436>, 2005.

846 Koffi, B., Schulz, M., Bréon, F. M., Griesfeller, J., Winker, D., Balkanski, Y., Bauer, S.,

847 Berntsen, T., Chin, M., Collins, W. D., Dentener, F., Diehl, T., Easter, R., Ghan, S., Ginoux, P.,
848 Gong, S., Horowitz, L. W., Iversen, T., Kirkevg, A., Koch, D., Krol, M., Myhre, G., Stier, P., and
849 Takemura, T.: Application of the CALIOP layer product to evaluate the vertical distribution of
850 aerosols estimated by global models: AeroCom phase i results,
851 <https://doi.org/10.1029/2011JD016858>, 2012.

852 Kok, J. F., Ridley, D. A., Zhou, Q., Miller, R. L., Zhao, C., Heald, C. L., Ward, D. S.,
853 Albani, S., and Haustein, K.: Smaller desert dust cooling effect estimated from analysis of dust
854 size and abundance, *Nat. Geosci.*, 10, 274–278, <https://doi.org/10.1038/Ngeo2912>, 2017.

855 Li, F., Vogelmann, A. M., and Ramanathan, V.: Saharan dust aerosol radiative forcing
856 measured from space, *J. Clim.*, 17, 2558–2571, [https://doi.org/Doi 10.1175/1520-0442\(2004\)017<2558:Sdarfm>2.0.Co;2](https://doi.org/Doi 10.1175/1520-0442(2004)017<2558:Sdarfm>2.0.Co;2), 2004.

858 Mahowald, N., Albani, S., Kok, J. F., Engelstaeder, S., Scanza, R., Ward, D. S., and Flanner,
859 M. G.: The size distribution of desert dust aerosols and its impact on the Earth system,
860 <https://doi.org/10.1016/j.aeolia.2013.09.002>, 1 December 2014.

861 Meloni, D., di Sarra, A., Di Iorio, T., and Fiocco, G.: Influence of the vertical profile of
862 Saharan dust on the visible direct radiative forcing, *J. Quant. Spectrosc. Radiat. Transf.*, 93, 397–
863 413, <https://doi.org/10.1016/j.jqsrt.2004.08.035>, 2005.

864 Meloni, D., Junkermann, W., di Sarra, A., Cacciani, M., De Silvestri, L., Di Iorio, T.,
865 Estellés, V., Gómez-Amo, J. L., Pace, G., and Sferlazzo, D. M.: Altitude-resolved shortwave and
866 longwave radiative effects of desert dust in the Mediterranean during the GAMARF campaign:
867 Indications of a net daily cooling in the dust layer, *J. Geophys. Res.*, 120, 3386–3407,
868 <https://doi.org/10.1002/2014JD022312>, 2015.

869 Meng, Z. K., Yang, P., Kattawar, G. W., Bi, L., Liou, K. N., and Laszlo, I.: Single-
870 scattering properties of tri-axial ellipsoidal mineral dust aerosols: A database for application to
871 radiative transfer calculations, *J. Aerosol Sci.*, 41, 501–512,
872 <https://doi.org/10.1016/j.jaerosci.2010.02.008>, 2010.

873 Mlawer, E. J. and Clough, S. A.: Shortwave and longwave enhancements in the rapid
874 radiative transfer model, *Proc. Seventh Atmos. Radiat. Meas. Sci. Team Meet.*, 409–413, 1998.

875 Mlawer, E. J., Taubman, S. J., Brown, P. D., Iacono, M. J., and Clough, S. A.: Radiative
876 transfer for inhomogeneous atmospheres: RRTM, a validated correlated-k model for the longwave,
877 *J. Geophys. Res. Atmos.*, 102, 16663–16682, <https://doi.org/10.1029/97jd00237>, 1997.

878 Myhre, G., Grini, A., Haywood, J. M., Stordal, F., Chatenet, B., Tanre, D., Sundet, J. K.,
879 and Isaksen, I. S. A.: Modeling the radiative impact of mineral dust during the Saharan Dust
880 Experiment (SHADE) campaign, *J. Geophys. Res.*, 108, <https://doi.org/Artn 8579>
881 [10.1029/2002jd002566](https://doi.org/10.1029/2002jd002566), 2003.

882 Myhre, G., Samset, B. H., Mohr, C. W., Alterskjær, K., Balkanski, Y., Bellouin, N., Chin,
883 M., Haywood, J., Hodnebrog, O., Kinne, S., Lin, G., Lund, M. T., Penner, J. E., Schulz, M.,
884 Schutgens, N., Skeie, R. B., Stier, P., Takemura, T., and Zhang, K.: Cloudy-sky contributions to
885 the direct aerosol effect, *Atmos. Chem. Phys.*, 20, 8855–8865, <https://doi.org/10.5194/acp-20-8855-2020>, 2020.

887 Patadia, F., Yang, E. S., and Christopher, S. A.: Does dust change the clear sky top of
888 atmosphere shortwave flux over high surface reflectance regions?, *Geophys. Res. Lett.*, 36,
889 <https://doi.org/10.1029/2009GL039092>, 2009.

890 Pu, B. and Ginoux, P.: How reliable are CMIP5 models in simulating dust optical depth?,
891 *Atmos. Chem. Phys.*, 18, 12491–12510, <https://doi.org/10.5194/acp-18-12491-2018>, 2018.

892 Raisanen, P., Haapanala, P., Chung, C. E., Kahnert, M., Makkonen, R., Tonttila, J., and

893 Nousiainen, T.: Impact of dust particle non-sphericity on climate simulations, *Q. J. R. Meteorol.*
894 *Soc.*, 139, 2222–2232, <https://doi.org/10.1002/qj.2084>, 2013.

895 Remer, L. A., Kaufman, Y. J., Tanré, D., Mattoo, S., Chu, D. A., Martins, J. V., Li, R. R.,
896 Ichoku, C., Levy, R. C., Kleidman, R. G., Eck, T. F., Vermote, E., and Holben, B. N.: The MODIS
897 aerosol algorithm, products, and validation, *J. Atmos. Sci.*, 62, 947–973,
898 <https://doi.org/10.1175/JAS3385.1>, 2005.

899 Ryder, C. L., Highwood, E. J., Lai, T. M., Sodemann, H., and Marsham, J. H.: Impact of
900 atmospheric transport on the evolution of microphysical and optical properties of Saharan dust,
901 *Geophys. Res. Lett.*, 40, 2433–2438, <https://doi.org/10.1002/grl.50482>, 2013a.

902 Ryder, C. L., Highwood, E. J., Rosenberg, P. D., Trembath, J., Brooke, J. K., Bart, M.,
903 Dean, A., Crosier, J., Dorsey, J., Brindley, H., Banks, J., Marsham, J. H., McQuaid, J. B.,
904 Sodemann, H., and Washington, R.: Optical properties of Saharan dust aerosol and contribution
905 from the coarse mode as measured during the Fennec 2011 aircraft campaign, *Atmos. Chem. Phys.*,
906 13, 303–325, <https://doi.org/10.5194/acp-13-303-2013>, 2013b.

907 Ryder, C. L., Marengo, F., Brooke, J. K., Estelles, V., Cotton, R., Formenti, P., McQuaid,
908 J. B., Price, H. C., Liu, D., Ausset, P., Rosenberg, P. D., Taylor, J. W., Choularton, T., Bower, K.,
909 Coe, H., Gallagher, M., Crosier, J., Lloyd, G., Highwood, E. J., and Murray, B. J.: Coarse-mode
910 mineral dust size distributions, composition and optical properties from AER-D aircraft
911 measurements over the tropical eastern Atlantic, *Atmos. Chem. Phys.*, 18, 17225–17257,
912 <https://doi.org/10.5194/acp-18-17225-2018>, 2018.

913 Ryder, C. L., Highwood, E. J., Walser, A., Seibert, P., Philipp, A., and Weinzierl, B.:
914 Coarse and Giant Particles are Ubiquitous in Saharan Dust Export Regions and are Radiatively
915 Significant over the Sahara, *Atmos. Chem. Phys. Discuss.*, <https://doi.org/10.5194/acp-2019-421>,
916 2019.

917 Sakai, T., Nagai, T., Zaizen, Y., and Mano, Y.: Backscattering linear depolarization ratio
918 measurements of mineral, sea-salt, and ammonium sulfate particles simulated in a laboratory
919 chamber, *Appl. Opt.*, 49, 4441–4449, 2010.

920 Satheesh, S. K. and Ramanathan, V.: Large differences in tropical aerosol forcing at the
921 top of the atmosphere and Earth’s surface, *Nature*, 405, 60–63, <https://doi.org/10.1038/35011039>,
922 2000.

923 Sinyuk, A., Torres, O., and Dubovik, O.: Combined use of satellite and surface
924 observations to infer the imaginary part of refractive index of Saharan dust, *Geophys. Res. Lett.*,
925 30, <https://doi.org/10.1029/2002GL016189>, 2003.

926 Sokolik, I. N., Toon, O. B., and Bergstrom, R. W.: Modeling the radiative characteristics
927 of airborne mineral aerosols at infrared wavelengths, *J. Geophys. Res.*, 103, 8813–8826,
928 <https://doi.org/10.1029/98jd00049>, 1998.

929 Song, Q., Zhang, Z., Yu, H., Kato, S., Yang, P., Colarco, P., Remer, L. A., and Ryder, C.
930 L.: Net radiative effects of dust in the tropical North Atlantic based on integrated satellite
931 observations and in situ measurements, *Atmos. Chem. Phys.*, 18, <https://doi.org/10.5194/acp-18-11303-2018>, 2018.

933 Song, Q., Zhang, Z., Yu, H., Ginoux, P., and Shen, J.: Global dust optical depth climatology
934 derived from CALIOP and MODIS aerosol retrievals on decadal timescales: regional and
935 interannual variability, *Atmos. Chem. Phys.*, 21, 13369–13395, <https://doi.org/10.5194/acp-21-13369-2021>, 2021.

937 Stamnes, K., Tsay, S.-C., Wiscombe, W., and Jayaweera, K.: Numerically stable algorithm
938 for discrete-ordinate-method radiative transfer in multiple scattering and emitting layered media,

939 Appl. Opt., 27, 2502, <https://doi.org/10.1364/ao.27.002502>, 1988.

940 Tegen, I. and Lacis, A. A.: Modeling of particle size distribution and its influence on the
941 radiative properties of mineral dust aerosol, *J. Geophys. Res. Atmos.*, 101, 19237–19244,
942 <https://doi.org/10.1029/95jd03610>, 1996.

943 Tegen, I., Lacis, A. A., and Fung, I.: The influence on climate forcing of mineral aerosols
944 from disturbed soils, *Nature*, 380, 419–422, <https://doi.org/10.1038/380419a0>, 1996.

945 Textor, C., Schulz, M., Guibert, S., Kinne, S., Balkanski, Y., Bauer, S., Bernsten, T.,
946 Berglen, T., Boucher, O., Chin, M., Dentener, F., Diehl, T., Easter, R., Feichter, H., Fillmore, D.,
947 Ghan, S., Ginoux, P., Gong, S., Kristjansson, J. E., Krol, M., Lauer, A., Lamarque, J. F., Liu, X.,
948 Montanaro, V., Myhre, G., Penner, J., Pitari, G., Reddy, S., Seland, O., Stier, P., Takemura, T.,
949 and Tie, X.: Analysis and quantification of the diversities of aerosol life cycles within AeroCom,
950 *Atmos. Chem. Phys.*, 6, 1777–1813, 2006.

951 Twomey, S.: The influence of pollution on the shortwave albedo of clouds, *J. Atmos. Sci.*,
952 34, 1149–1152, 1977.

953 Voss, K. K. and Evan, A. T.: A New Satellite-Based Global Climatology of Dust Aerosol
954 Optical Depth, *J. Appl. Meteorol. Climatol.*, 59, 83–102, <https://doi.org/10.1175/JAMC-D-19>,
955 2020.

956 Vouk, V.: Projected area of convex bodies [3], <https://doi.org/10.1038/162330a0>, 1948.

957 Weinzierl, B., Ansmann, A., Prospero, J. M., Althausen, D., Benker, N., Chouza, F.,
958 Dollner, M., Farrell, D., Fomba, W. K., Freudenthaler, V., Gasteiger, J., Gross, S., Haarig, M.,
959 Heinold, B., Kandler, K., Kristensen, T. B., Mayol-Bracero, O. L., Muller, T., Reitebuch, O., Sauer,
960 D., Schafler, A., Schepanski, K., Spanu, A., Tegen, I., Toledano, C., and Walser, A.: THE
961 SAHARAN AEROSOL LONG-RANGE TRANSPORT AND AEROSOL-CLOUD-
962 INTERACTION EXPERIMENT Overview and Selected Highlights, *Bull. Am. Meteorol. Soc.*,
963 98, 1427–1451, <https://doi.org/10.1175/Bams-D-15-00142.1>, 2017.

964 Winker, D. M., Vaughan, M. A., Omar, A., Hu, Y., Powell, K. A., Liu, Z., Hunt, W. H.,
965 and Young, S. A.: Overview of the CALIPSO mission and CALIOP data processing algorithms,
966 *J. Atmos. Ocean. Technol.*, 26, 2310–2323, <https://doi.org/10.1175/2009JTECHA1281.1>, 2009.

967 Wiscombe, W. J.: Improved Mie Scattering Algorithms, *Appl. Opt.*, 19, 1505–1509,
968 <https://doi.org/Doi.10.1364/Ao.19.001505>, 1980.

969 Wu, M., Liu, X., Yu, H., Wang, H., Shi, Y., Yang, K., Darmenov, A., Wu, C., Wang, Z.,
970 Luo, T., Feng, Y., and Ke, Z.: Understanding processes that control dust spatial distributions with
971 global climate models and satellite observations, *Atmos. Chem. Phys.*, 20, 13835–13855,
972 <https://doi.org/10.5194/acp-20-13835-2020>, 2020.

973 Yu, H., Kaufman, Y. J., Chin, M., Feingold, G., Remer, L. A., Anderson, T. L., Balkanski,
974 Y., Bellouin, N., Boucher, O., Christopher, S., DeCola, P., Kahn, R., Koch, D., Loeb, N., Reddy,
975 M. S., Schulz, M., Takemura, T., and Zhou, M.: A review of measurement-based assessments of
976 the aerosol direct radiative effect and forcing, *Atmos. Chem. Phys.*, 6, 613–666, 2006.

977 Yu, H., Chin, M., Remer, L. A., Kleidman, R. G., Bellouin, N., Bian, H., and Diehl, T.:
978 Variability of marine aerosol fine-mode fraction and estimates of anthropogenic aerosol
979 component over cloud-free oceans from the Moderate Resolution Imaging Spectroradiometer
980 (MODIS), *J. Geophys. Res. Atmos.*, 114, <https://doi.org/10.1029/2008JD010648>, 2009.

981 Yu, H., Chin, M., Winker, D. M., Omar, A. H., Liu, Z., Kittaka, C., and Diehl, T.: Global
982 view of aerosol vertical distributions from CALIPSO lidar measurements and GOCART
983 simulations: Regional and seasonal variations, *J. Geophys. Res. Atmos.*, 115, 1–19,
984 <https://doi.org/10.1029/2009JD013364>, 2010.

985 Yu, H., Tan, Q., Chin, M., Remer, L. A., Kahn, R. A., Bian, H., Kim, D., Zhang, Z., Yuan,
986 T., Omar, A. H., Winker, D. M., Levy, R. C., Kalashnikova, O., Crepeau, L., Capelle, V., and
987 Chédin, A.: Estimates of African Dust Deposition Along the Trans-Atlantic Transit Using the
988 Decadelong Record of Aerosol Measurements from CALIOP, MODIS, MISR, and IASI, *J.*
989 *Geophys. Res. Atmos.*, 124, 7975–7996, <https://doi.org/10.1029/2019JD030574>, 2019.

990 Yu, H., Yang, Y., Wang, H., Tan, Q., Chin, M., Levy, R., Remer, L., Smith, S., Yuan, T.,
991 and Shi, Y.: Interannual Variability and Trends of Combustion Aerosol and Dust in Major
992 Continental Outflows Revealed by MODIS Retrievals and CAM5 Simulations During 2003–2017,
993 *Atmos. Chem. Phys. Discuss.*, 1–38, <https://doi.org/10.5194/acp-2019-621>, 2020.

994 Zhang, J. L. and Christopher, S. A.: Longwave radiative forcing of Saharan dust aerosols
995 estimated from MODIS, MISR, and CERES observations on Terra, *Geophys. Res. Lett.*, 30,
996 <https://doi.org/Artn 2188> 10.1029/2003gl018479, 2003.

997 Zhang, Z. B., Meyer, K., Yu, H. B., Platnick, S., Colarco, P., Liu, Z. Y., and Oreopoulos,
998 L.: Shortwave direct radiative effects of above-cloud aerosols over global oceans derived from 8
999 years of CALIOP and MODIS observations, *Atmos. Chem. Phys.*, 16, 2877–2900,
1000 <https://doi.org/10.5194/acp-16-2877-2016>, 2016.

1001 Zhao, C., Liu, X., Leung, L. R., Johnson, B., McFarlane, S. A., Gustafson, W. I., Fast, J.
1002 D., and Easter, R.: The spatial distribution of mineral dust and its shortwave radiative forcing over
1003 North Africa: Modeling sensitivities to dust emissions and aerosol size treatments, *Atmos. Chem.*
1004 *Phys.*, 10, 8821–8838, <https://doi.org/10.5194/acp-10-8821-2010>, 2010.

1005 Zheng, J., Zhang, Z., Garnier, A., Yu, H., Song, Q., Wang, C., Dubuisson, P., and Di Biagio,
1006 C.: The thermal infrared optical depth of mineral dust retrieved from integrated CALIOP and IIR
1007 observations, *Remote Sens. Environ.*, 270, <https://doi.org/10.1016/j.rse.2021.112841>, 2022.

1008 Zhou, M., Yu, H., Dickinson, R. E., Dubovik, O., and Holben, B. N.: A normalized
1009 description of the direct effect of key aerosol types on solar radiation as estimated from Aerosol
1010 Robotic Network aerosols and Moderate Resolution Imaging Spectroradiometer albedos, *J.*
1011 *Geophys. Res. D Atmos.*, 110, 1–10, <https://doi.org/10.1029/2005JD005909>, 2005.

1012